Coexistence of five domains at single propagating interface in single-crystal Ni-Mn-Ga shape memory alloy

Chengguan Zhang, Xavier Balandraud, Yongjun He

Coexistence of five domains at single propagating interface in single-crystal Ni-Mn-Ga Shape Memory Alloy

Chengguan Zhang [1], Xavier Balandraud [2], Yongjun He [1]*

[1] UME, ENSTA Paris, Institut Polytechnique de Paris, Palaiseau 91120, France

[2] CNRS, Clermont Auvergne Université, Clermont Auvergne INP, Institut Pascal, Clermont-Ferrand F-63000, France

*Corresponding author: Yongjun He

yongjun.he@ensta-paris.fr

Abstract

Coexistence of both austenite and martensite during phase transformation is a common feature of all Shape Memory Alloys (SMAs). The martensite has different variants featuring characteristic deformations rotationally linked to each other due to the symmetries of the austenite parent phase, and can form twins by mixing pair of variants which lead to different mean characteristic deformations. Multiple-domain microstructures (consisting of austenite, martensite twins and individual martensite variants) evolve collectively within an SMA sample during the phase transformation, contributing thus to the material's macroscopic response (e.g., its global deformation). Particularly, the multiple domains can exist at the diffuse austenite-martensite interface nucleating and propagating in a single crystal in certain conditions. This implies an energy barrier for this interfacial structure, influencing the interface kinetics and the driving force (energy dissipation) of the phase transformation. In this paper, we report an experimentally observed interface consisting of five domains (austenite, one martensite variant and three twins) in a Ni-Mn-Ga single-crystal initially consisting of one martensite variant and subjected to a uniaxial thermal gradient. The compatibility analysis (performed from the characteristic strains of the three martensite variants having approximately a tetragonal symmetry) reveals that the five-

domain interface is not a perfectly compatible pattern like the basic habit plane (consisting of only one twin compatible with austenite). However, its level of non-compatibility is similar to that of the quite common X-interface (four-domain coexistence) which is observed in many SMAs. Further, the significant effects of the thermal loading path and the material initial state (the initial martensite variant) on the domain pattern formation are demonstrated and analyzed. The experimental observation and the theoretical analysis of the domain patterns can provide hints to better understand diffuse interface kinetics and phase transformation hysteresis.

Keywords: microstructures, phase transformation, twinning, strain compatibility, martensite

1. Introduction

The superelasticity/pseudoelasticity and shape memory effect of shape memory alloys (SMAs) result from a 1st-order solid-solid phase transformation (martensitic transformation) that can be induced by thermal, mechanical, and magnetic loadings (Kiefer and Lagoudas, 2005; Arndt et al., 2006; Karaca et al., 2006; Sehitoglu et al., 2012; Chen et al., 2014; Haldar et al., 2014; Kamarád et al., 2014; Pascan et al., 2015; Cisse et al., 2016; Heczko et al., 2016; Rogovoy and Stolbova, 2016; Yin et al., 2016; Bruno et al., 2017; Zhang et al., 2018b; Chen and He, 2020; Zhang et al., 2020). The high-temperature stable parent phase (*austenite*) has cubic symmetry whereas the low-temperature stable product phase (*martensite*) has lower symmetry, such as tetragonal, orthorhombic, and monoclinic symmetry, depending on the chemical composition. Martensite appears in the form of several *variants* with different orientations with respect to the austenite parent crystal, and therefore different characteristic transformation strains (Bain strains) are resulted (Ball and James, 1989; M. Pitteri and Zanzotto, 1998; James and Hane, 2000; Pitteri and Zanzotto, 2002; Bhattacharya, 2003). According to equilibrium thermomechanics (Ericksen, 1975; Falk, 1980; James, 1980; Abeyaratne and Knowles, 1991; He and Sun, 2009; Duval et al., 2011; Hallai and Kyriakides, 2013) and the experimental observations (Segui et al., 1996; Glatz et al., 2009; Seiner and Landa, 2009; Seiner, 2015; Zhang et al., 2020; Qin et al., 2023; Zhang et al., 2023), the martensite variants and austenite with equal free energy can coexist during the phase transformation, among which there are twin boundaries (separating different martensite variants) and habit planes (separating austenite from martensite twins or variants). To guarantee the

deformation reversibility of the phase transformation (avoiding plasticity), the twin boundaries and the habit planes must be compatible (coherent), meaning that the characteristic transformation strains of the different domains (martensite variants, twins, and austenite) must be accommodated without elastic strain (called "perfectly compatible" domain patterns) or with only small elastic strains (so-called "non-perfectly compatible" domain patterns). In both cases (with or without elasticity), the displacement continuity is guaranteed when crossing the twin boundaries or the habit planes, satisfying the Hadamard equation (Ball and James, 1989; Bhattacharya, 2003). Based on the pioneering work in understanding the basic kinematics and energetics in 1950-1989 (Bowles, 1951; Wechsler et al., 1953; Basinski and Christian, 1954; Bowles and Mackenzie, 1954; Roitburd, 1978; Ericksen, 1980; Khachaturyan, 1983; Barsh and Krumhansl, 1984; Pitteri, 1984; Ball and James, 1989; Krumhansl and Gooding, 1989), various interfacial structures, especially the non-perfectly compatible domain patterns, have been intensively studied from 1990 until now (Bhattacharya, 1991; Bhattacharya, 1992; Ruddock, 1994; Shield, 1995; Ball and Carstensen, 1997; Hane and Shield, 1998; M. Pitteri and Zanzotto, 1998; Hane, 1999; Hane and Shield, 1999b; Hane and Shield, 1999a; Hane and Shield, 2000a; Hane and Shield, 2000b; Balandraud and Zanzotto, 2007; Stupkiewicz et al., 2007; Seiner et al., 2008; Seiner et al., 2009; Seiner and Landa, 2009; Balandraud et al., 2010; Levitas et al., 2010; Stupkiewicz and Górzyńska-Lengiewicz, 2012; Stupkiewicz et al., 2012; Seiner et al., 2014; Seiner, 2015; Bronstein et al., 2019; Seiner et al., 2020; Stupkiewicz et al., 2021; He, 2023; Qin et al., 2023; Zhang et al., 2023).

Particularly, the domain patterns in single-crystal SMAs can clearly indicate the material's crystallographic relations and the associated compatibility requirements. For example, in clean single-crystals with little defects (such as annealed specimens in (Chang and Read, 1951)), the martensitic phase transformation can occur via a single interface propagation passing through a single-crystal specimen under thermal loadings such as a temperature gradient (Basinski and Christian, 1954; Salzbrenner and Cohen, 1979; Christian, 1982; Seiner et al., 2008; He, 2023; Qin et al., 2023; Zhang et al., 2023). The propagating interface can have different structures as classified in Fig. 1.

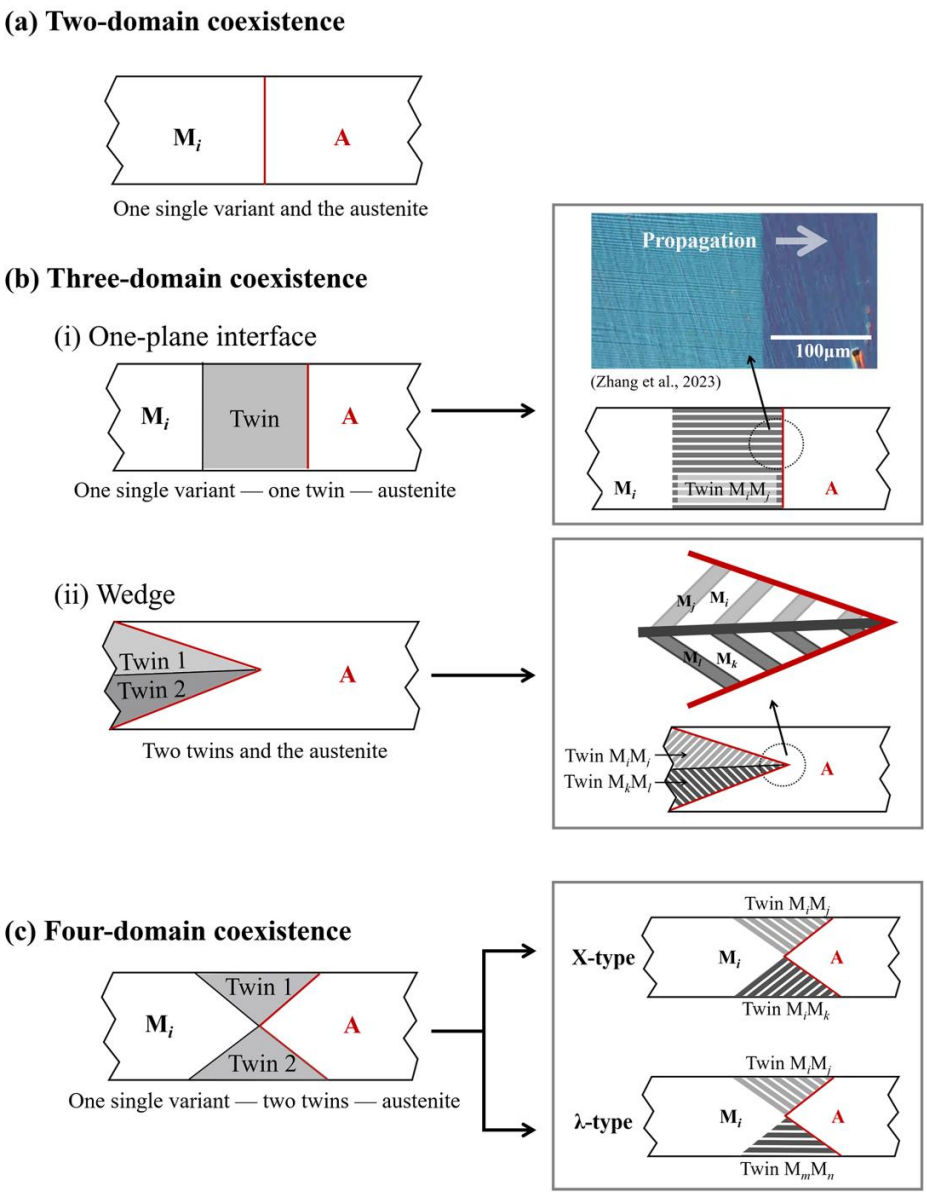

Fig. 1 Typical multiple-domain coexistence reported in literature; a domain represents a region where the macroscopic strain is approximately uniform.

In the extremely ideal case (the simplest interfacial structure), only two domains coexist during the phase transformation as shown in Fig. 1(a) where the austenite domain is separated by an atomistically sharp interface from a single martensite variant M_i (the i^{th} variant of the martensite

phase). This ideal case is rare in experiments and its requirement on the material's lattice parameters is very strict, such as the "middle eigenvalue equal to 1" and "cofactor condition" (Cui et al., 2006; Chen et al., 2013; Gu et al., 2018). The case of a martensite variant perfectly compatible with austenite leads to many interesting features, such as extremely low hysteresis and ultra-high fatigue life.

By contrast, three-domain coexistence is more common in experiments; see Fig. 1(b) where two basic patterns are shown: (1) Planar interface (one habit plane) involving the austenite, a twin laminate and a single martensite variant, whose detailed evolutions in experiments can be found in the movies of (Qin et al., 2023; Zhang et al., 2023); it has been verified by compatibility analysis that this planar-interface domain pattern is energy-minimizing (Ball and James, 1989; Bhattacharya, 2003; Bronstein et al., 2019; Seiner et al., 2020). (2) "Wedge" pattern involving an austenite domain and two different martensite twins (Otsuka and Shimizu, 1974; Saburi and Wayman, 1979; Shusong Tan and Xu, 1990; Bhattacharya, 1991; Otsuka and Wayman, 1998; Bhattacharya, 2003). The wedge microstructure might not be perfectly compatible according to the theory of Ball and James (Bhattacharya, 1991; Balandraud and Zanzotto, 2007; Balandraud et al., 2010), but it is still energy minimizing according to the more general theory in (Ruddock, 1994). This means that the three-domain coexistence corresponds to a perfectly or nearly-perfectly compatible domain pattern without the strict requirement on material's lattice parameters. Thus, the three-domain coexistence are often observed in experiments.

Besides the three-domain coexistence, four-domain coexistence is also frequently observed in experiments; see Fig. 1(c) where the austenite, two twins and a single martensite variant M_i coexist (Basinski and Christian, 1954; Bhattacharya, 2003; Seiner et al., 2008; Seiner, 2015; Qin et al., 2023). There are two typical patterns: X-interface and λ-interface; they can be distinguished by the orientations of the twin boundaries and the contact surfaces between the single martensite variant and the twins. For example, if any one of the twins has its twin boundary *not* parallel to its contact surface with the single variant M_i, the four-domain pattern is called λ-interface. Otherwise, the four-domain pattern is called X-interface (Seiner et al., 2008). As demonstrated in the general theory of (Ruddock, 1994) and in the analysis of (Glatz et al., 2009; Seiner et al., 2009), the four-domain pattern (particularly the X-interface) is a non-perfectly compatible structure. That means there is elastic energy stored in this interfacial structure. As mentioned in (Ruddock, 1994), such

non-perfectly compatible structure might appear under high driving forces such as a high temperature gradient.

From the above overview, we can see that the simplest pattern (two-domain coexistence) with small driving force (low hysteresis) can appear only in special materials whose lattice parameters satisfy strict conditions (Cui et al., 2006; Chen et al., 2013; Gu et al., 2018). By contrast, the medium complex pattern (three-domain coexistence) can be observed in most SMAs and under most loading conditions. More complex patterns (four-domain coexistence) are expected to appear with high driving force to overcome the energy barrier, i.e., the elastic energy stored in the non-perfectly compatible interfacial structures. It is implied that the interfacial structure and the associated stored energy are closely related to the interface kinetics and the energy dissipation of the phase transformation. Detailed discussion on the relation between the interfacial energy and the phase-transformation hysteresis can be found in (Müller, 1989; Müller and Xu, 1991; Sun and He, 2008; Zhang et al., 2009; Petryk and Stupkiewicz, 2010; He, 2023).

Thus, a question naturally rises: is it possible for the propagating interface to have a more complex pattern? The answer is yes. In Section 2 of this paper, we report a recently observed pattern of five-domain coexistence in a propagating interface in Ni-Mn-Ga single-crystal SMA as shown in Fig. 2(a) where we identified the austenite, a single variant M_3 and three twins: Twin M_3M_2 consisting of two martensite variants M_3 and M_2 whose volume fractions are around 2/3 and 1/3 respectively; Twins M_3M_1 and M_1M_3 with the same components M_1 and M_3, but their major component with 2/3 volume fraction is different (M_3M_1's major component is M_3 while that of M_1M_3 is M_1). Although the material has three martensite variants with approximately tetragonal symmetry (Murray et al., 2000; Heczko et al., 2002; Zhang et al., 2018a) and its phase transformation has been intensively studied under different thermal, mechanical and magnetic loadings (James, 1980; James et al., 1995b; James et al., 1995a; Mañosa et al., 1997; Glavatska and Ullakko, 2000; James and Hane, 2000; Glavatska and Ullakko, 2001; Heczko et al., 2002; Karaman et al., 2006; Planes et al., 2007; Heczko et al., 2013; Haldar et al., 2014; Heczko et al., 2016; Heczko et al., 2018; Zhang et al., 2018a, b; Chen and He, 2020), its interfacial microstructures have not yet been systematically investigated. To the best knowledge of the authors, there is no report in literature about a five-domain coexistence of propagating interface in Ni-Mn-Ga single-crystal SMA. To understand this new pattern, compatibility analysis is

performed in Section 3, where we combine the spirit of (Balandraud and Zanzotto, 2007; Balandraud et al., 2010) and (Glatz et al., 2009; Seiner et al., 2009) to characterize the interfacial structure's non-compatibility with three "indicators" (three angles). Comparison is also made with the four-domain interface (X-interface). Then, the reasons for the new pattern formation are given from considerations about the thermal loading path and the material initial state (the initial martensite variant). The implications of the multi-domain observation and the theoretical analysis are discussed in Section 4. Final conclusions are given in Section 5.

2. Experimental observation

The specimen used in the current study is a $Ni_{50}Mn_{28}Ga_{22}$ (at. %) single-crystal rectangular bar (from ETO, Germany) with the size of 20 mm (length) × 2.5 mm (width) × 1 mm (thickness) along *x*, *y*, and *z* directions respectively. It was cut approximately along the {100} planes of the cubic austenite crystal. The material's characteristic transformation temperatures M_s, M_f, A_s, and A_f, are 48 ℃, 45 ℃, 52 ℃, and 55 ℃, respectively, measured by DSC (Differential Scanning Calorimetry). So, the material is in the martensite state at room temperature (around 23 ^{o}C). According to (Murray et al., 2000; Heczko et al., 2002; Zhang et al., 2018a), the martensite variants can be considered to have approximately tetragonal symmetry with two long axes (denoted as '*a*') and a short axis (denoted as '*c*') while the lattice parameter of the cubic austenite is denoted as "a_0" as shown in Fig. 2(a). In this study, the utilized lattice parameters are: $a \approx 5.95$ Å, $c \approx 5.61$ Å, and $a_0 \approx 5.84$ Å (Murray et al., 2000; Heczko et al., 2002; Zhang et al., 2018a).

The experimental setup is shown in Fig. 2(b). It can be noted that the two ends of the specimen are supported by two plates, one in aluminum alloy connected to a heater (changing the temperature from room temperature to above 100 ^{o}C) and the other made of plastic foam to avoid strong constraint (i.e., the specimen can freely extend or shrink during the phase transformation). Thus, the temperature-induced $M_3 \rightarrow A$ transformation occurs via an interface propagating from the specimen's right end to the left end. To capture the interfacial structure, an optical microscope (AX70 Olympus, Japan) equipped with polarized light is adopted to observe the mechanically polished specimen's top surface (*x*-*y* plane), corresponding to the (100) plane of the cubic austenite crystal. Via the optical microscope, the evolution of the propagating interface is recorded by a

camera (OV48C, OmniVision, China). Before the test (at room temperature), the specimen was compressed along its *z*-axis to become single martensite variant M_3. During the heating at the specimen's right end, a diffuse interface corresponding to a five-domain coexistence passes through the region observed by the microscope (from right to left); see the movies 1~3 in supplementary material. whose typical frames are given in Fig. 2.

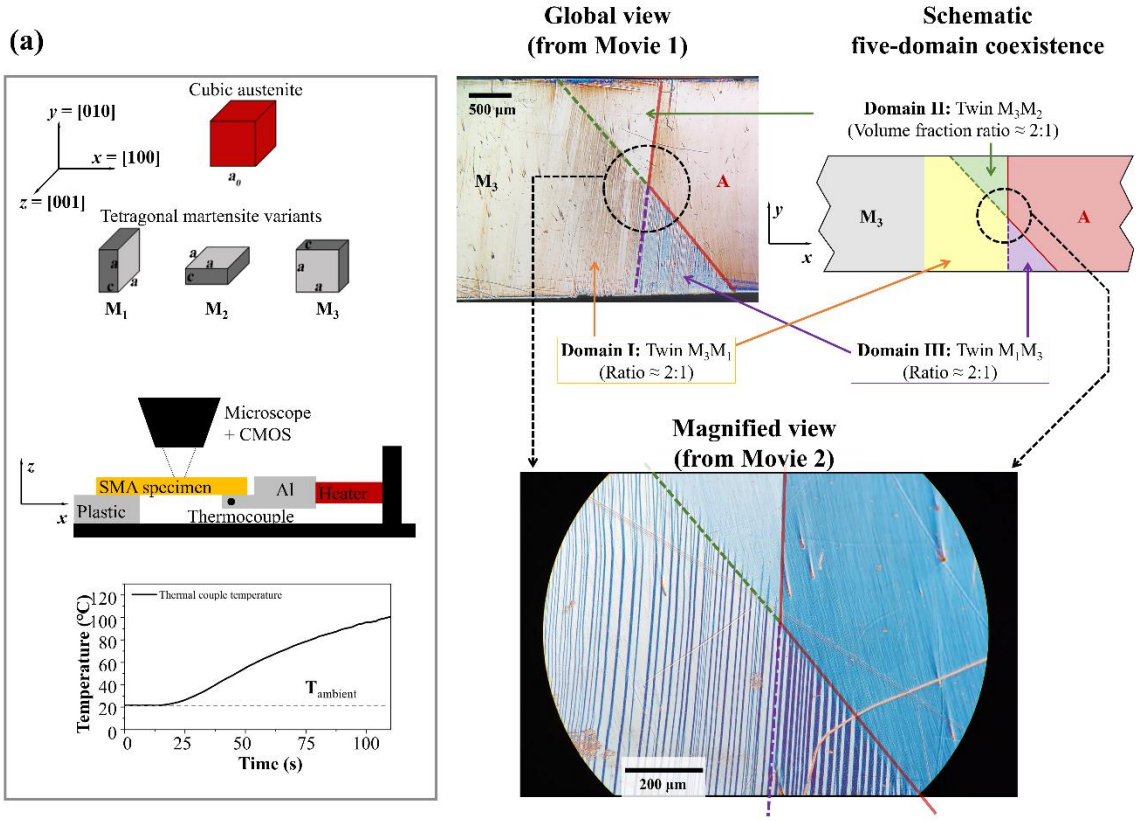
(a)
Cubic austenite
y = [010]
x = [100]
z = [001]
Tetragonal martensite variants
M1
M2
M3
Microscope
+ CMOS
SMA specimen
Al
Heater
Plastic
Thermocouple
Thermal couple temperature
Temperature (°C)
Time (s)
T ambient
Global view
(from Movie 1)
Schematic
five-domain coexistence
500 µm
M3
A
Domain II: Twin M3M2
(Volume fraction ratio ≈ 2:1)
Domain I: Twin M3M1
(Ratio ≈ 2:1)
Domain III: Twin M1M3
(Ratio ≈ 2:1)
Magnified view
(from Movie 2)
200 µm

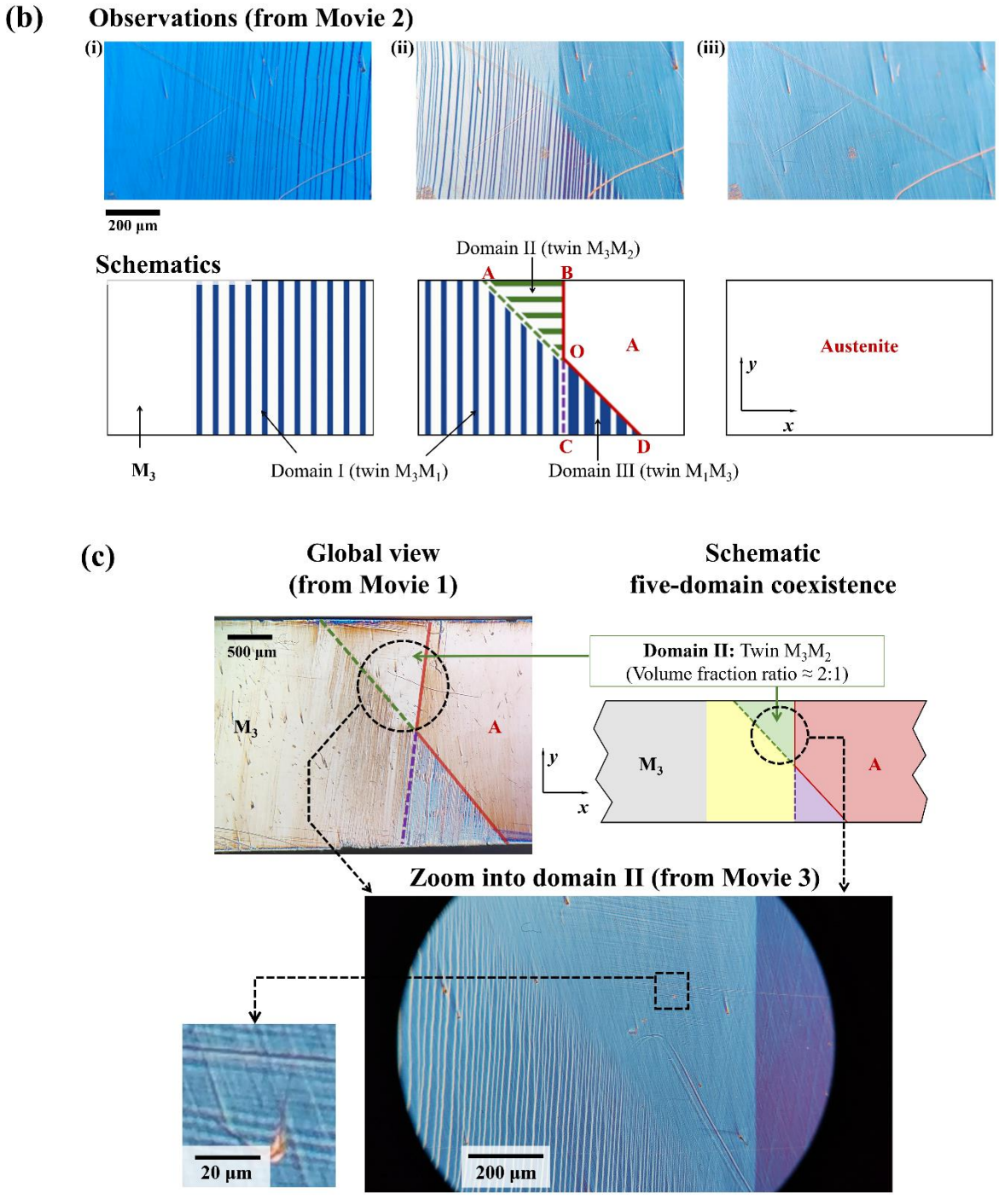

Fig.2 The experimental evidence of a five-domain coexistence during the heating-driven interface propagation in a Ni-Mn-Ga single crystal: a) Experiment and associated observation from Movies 1 and 2 in supplementary material; (b) Representative frames (at 3.63s, 7.16s and 10s) of the Movie

2 about the domains' detailed evolution; (c) Magnified view (ii) from Movie 3 showing nearly horizontal laminates in Domain II.

Movie 1 demonstrates the propagation of the five-domain configuration along the specimen while Movie 2 is a zoom to show the detailed evolution of the domains (see also the global view and the magnified view in Fig. 2(a)). Three typical frames of Movie 2 are shown in Fig. 2(b). It can be seen from Frame (i) that, when the diffuse interface approaches from the right, some narrow bands (vertical lines) appear in the domain of single variant M_3 (the initial state of the specimen), forming thus a twin laminate referred to as Domain I. Further, Frame (ii) shows domains II and III and austenite besides domain I. It is seen that domains I and III have similarities: indeed, both have vertical lines (bands); but they have different fractions of bright and dark. Finally, Frame (iii) shows a uniform region, which should be austenite. In fact, we can measure the mean strain field within each domain with DIC (Digital Image Correlation) to determine its state (austenite, single variant or twin) as discussed in details in (Qin et al., 2023; Zhang et al., 2023). On the other hand, we can also determine the domain's state by the combination of a simple compatibility analysis and the experimentally observed orientations of the domain walls (habit planes and the planes between different twins) and the twin-boundary orientation (the vertical lines in domains I and III) as shown in the following.

According to the simple compatibility analysis of the habit plane between austenite and a twin consisting of two tetragonal martensite variants (Zhang et al., 2018a; Qin et al., 2023), only six twins can have habit planes with austenite: M_1M_2, M_1M_3, M_2M_1, M_2M_3, M_3M_1 and M_3M_2, whose major component has the volume fraction of around 2/3; the traces (projections) of their habit planes and twin boundaries on the specimen's *x*-*y* surface are shown in Fig. 3. Strict derivation and quantification of the orientations of the habit planes and twin boundaries can be found in Appendix A. Now, from the comparison between Fig. 3 and Frame (ii) of Fig. 2(b), we can judge that the domain III with the vertical lines (twin boundaries) and the inclined trace of the habit plane (around 45^o) should be M_1M_3. As domain I is different from domain III (different fractions of bright and dark bands), but has the similar twin boundaries (vertical lines in the domains), domain I should be M_3M_1 (in fact we can use the software *Image J* to measure the fractions of the bright and dark bands). Then, the domain II in Frame (ii) of Fig. 2(b) needs to be compatible with both

austenite and domain I. Based on the vertical trace of the habit plane between the domain II and austenite (i.e., line OB in Fig. 2(b)), we judge that domain II is either M_3M_2 or M_1M_2. And the magnified view (ii) of the experimental observation in Fig. 2(c) shows nearly horizontal laminates in the domain II; so, the domain II must be M_3M_2 according to Fig. 3 (the twin M_3M_2 has horizontal laminates while the twin M_1M_2 has inclined laminates). Moreover, it is easy to theoretically verify that the twin M_3M_2 of domain II can be compatible with the domain I (twin M_3M_1) through the inclined domain wall (OA line around 45° to the *x*-axis in Fig. 2(b)). In addition, the DIC deformation measurements on the domain II have the strain components $\varepsilon_{xx} \approx 2\%$ and $\varepsilon_{yy} \approx 0\%$, which correspond to the average strain state of the twin M_3M_2. Detailed DIC strain measurements and discussions can be found in the Appendix C.

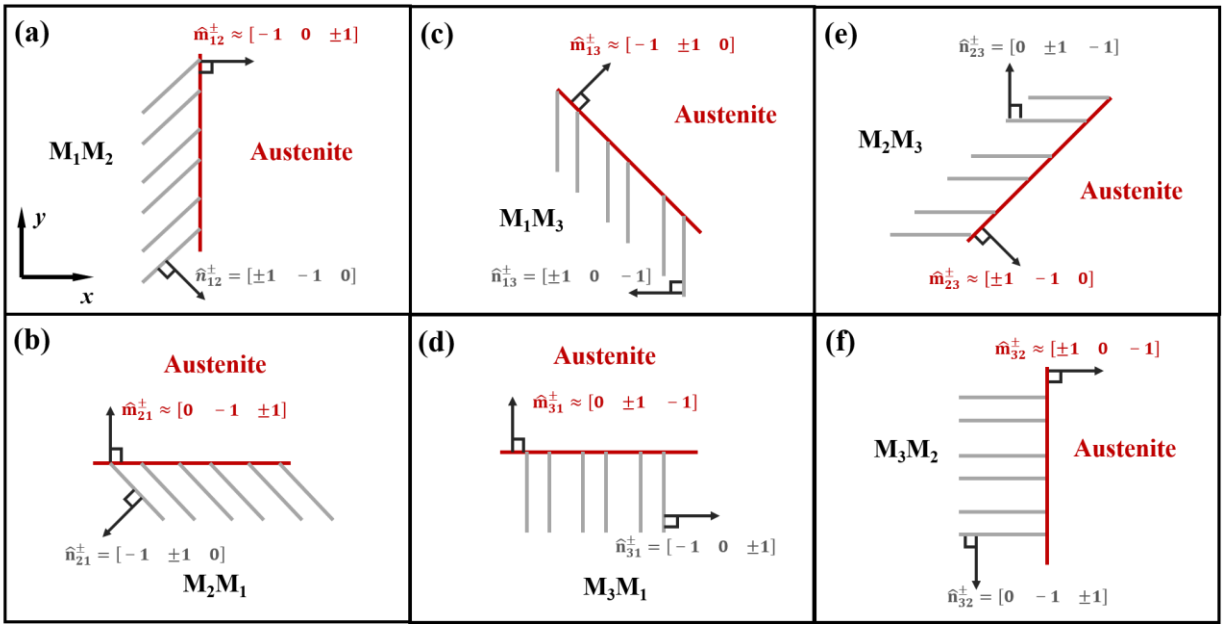

Fig. 3. The traces (projections) of the theoretically predicted habit planes and twin boundaries of the six possible twins on the specimen's *x*-*y* surface.

Thus, the main states of the domains are determined, but their global compatibility needs to be verified, because some rotation is needed for each compatible domain wall, and the rotations for all the compatible domain walls might restrict each other to generate non-compatibility

(causing elastic strain) as in the wedge and the X-interface (Balandraud and Zanzotto, 2007; Glatz et al., 2009; Seiner et al., 2009; Balandraud et al., 2010). In the next section, the compatibility analysis of the domain walls, and the characterization of the global compatibility are performed.

3. Compatibility analysis and the reason for five-domain formation

3.1 Hadamard jump condition and twinning equation

Hadamard jump condition, Eq. (1), applies to the following situation: two regions (originally connected by a plane) take different deformations and remain perfectly connected.

$$\mathbf{F}_{\mathrm{I}} - \mathbf{F}_{\mathrm{II}} = \mathbf{a} \otimes \hat{\mathbf{n}} \tag{1.}$$

where $\mathbf{F}_{\mathrm{I}}$ and $\mathbf{F}_{\mathrm{II}}$ are the two different deformation matrices (so-called deformation gradients); $\hat{\mathbf{n}}$ denotes the unit normal of the plane in the undeformed configuration, and **a** is a vector (so-called shear vector).

Concerning the cubic-to-tetragonal transformation in Ni-Mn-Ga single crystal, the austenite is taken as reference (described by an identify matrix **I**), and the characteristic deformations of the martensite variants are described by the three deformation matrices (so-called Bain matrices), $\mathbf{U}_i$ (i = 1, 2 or 3) in Eq. (2), corresponding to the three tetragonal variants in Fig. 2(a).

$$\mathbf{I} = \begin{pmatrix} 1 & 0 & 0 \\ 0 & 1 & 0 \\ 0 & 0 & 1 \end{pmatrix}, \quad \mathbf{U}_1 = \begin{pmatrix} \alpha & 0 & 0 \\ 0 & \beta & 0 \\ 0 & 0 & \beta \end{pmatrix}, \quad \mathbf{U}_2 = \begin{pmatrix} \beta & 0 & 0 \\ 0 & \alpha & 0 \\ 0 & 0 & \beta \end{pmatrix}, \quad \mathbf{U}_3 = \begin{pmatrix} \beta & 0 & 0 \\ 0 & \beta & 0 \\ 0 & 0 & \alpha \end{pmatrix} \tag{2.}$$

where α and β are the so-called transformation stretches that are derived from the lattice parameters of austenite and martensite as follows: $\alpha = c/a_0 = 0.9606$ and $\beta = a/a_0 = 1.0188$. Note that $0 < \alpha < 1 < \beta$ and $\det(\mathbf{U}_i) = 0.997 \approx 1$, meaning that the phase transformation is nearly isochoric.

Generally, if letting $\mathbf{F}_{\mathrm{I}}$ and $\mathbf{F}_{\mathrm{II}}$ directly equal to the Bain matrices of two different variants (U_i and U_j) respectively, there is no solution to Eq. (1). Normally, a rotation of a variant relative to the other variant is needed to achieve a compatible plane (twin boundary) between the two variants, satisfying the Hadamard jump condition as shown in Eq. (3):

$$\mathbf{Q}_{ij}\mathbf{U}_j - \mathbf{U}_{\mathrm{i}} = \mathbf{a}_{ij} \otimes \hat{\mathbf{n}}_{ij} \tag{3.}$$

where $\mathbf{Q}_{ij}$ is the rotation acting on $\mathbf{U}_j$ of the twin (consisting of the two variants $\mathbf{U}_i$ and $\mathbf{U}_j$), whose shear vector and unit plane normal are $\mathbf{a}_{ij}$ and $\hat{\mathbf{n}}_{ij}$, respectively. The procedures to solve the twinning equation (Eq. (3)) can be found in Appendix A and (Bhattacharya, 2003). The solutions to Eq. (3) for all the possible twins are summarized in Table A1 of Appendix A. Particularly, the orientations of the twin boundaries are schematically shown in Fig. 3 where the traces (or projections) of the twinning planes on the *x*-*y* surface are horizontal or vertical or inclined 45^o lines, agreeing with the current observation in Fig. 2 and other experiments (Qin et al., 2023; Zhang et al., 2023).

3.2 Compatibility of domain walls (habit planes and twin-twin planes)

After obtaining the pairs of compatible variants (particularly with the rotation $\mathbf{Q}_{ij}$ and the twinning plane unit normal $\hat{\mathbf{n}}_{ij}$), we can denote the average characteristic deformation matrix for the twin by $\mathbf{U}_{ij}$:

$$\mathbf{U}_{ij} = \lambda_{ij}\mathbf{U}_i + (1-\lambda_{ij})\,\mathbf{Q}_{ij}\mathbf{U}_j, \tag{4.}$$

where $\lambda_{ij} \geqslant 1/2$ is the volume fraction of the major component $\mathbf{U}_i$ in the twin (Note: the twin consisting of major component $\mathbf{U}_i$ and minor component $\mathbf{U}_j$ is denoted by $\mathbf{U}_{ij}$; the opposite case is denoted by $\mathbf{U}_{ji}$). Generally, λ_{ij} can only take certain values to achieve compatible domain walls: (1) the habit plane between austenite and a twin (such as the domain walls OB and OD in Fig. 2(b)), and (2) the twin-twin plane (such as the domain walls OA and OC in Fig. 2(b)). In the following, we formulate the compatibility for the two types of domain walls.

3.2.1 Habit plane

Similar to Eqs. (1) and (3), the compatibility equation of the habit plane can be written as:

$$\mathbf{F}_{ij} - \mathbf{I} = \mathbf{b}_{ij} \otimes \hat{\mathbf{m}}_{ij} \tag{5.}$$

here, $\mathbf{F}_{ij} = \mathbf{R}_{ij}\mathbf{U}_{ij}$ where $\mathbf{U}_{ij}$ is the average deformation matrix given by Eq. (4) and $\mathbf{R}_{ij}$ is the rotation acting on twin $\mathbf{U}_{ij}$; $\mathbf{b}_{ij}$ and $\hat{\mathbf{m}}_{ij}$ denote the shear vector and the habit-plane unit normal,

respectively. The procedure for solving Eqs. (4) and (5) to determine the rotation $\mathbf{R}_{ij}$, the volume fraction λ_{ij}, and the habit plane normal $\widehat{\mathbf{m}}_{ij}$ can be found in Appendix A and (Bhattacharya, 2003). The solutions for all the possible habit planes and the associated twins are listed in Table A2, whose schematics are shown in Fig. 3 where the traces (projections) of the habit planes on the specimen's *x*-*y* surface are *approximately* horizontal or vertical or inclined 45° lines, agreeing with the current observation in Fig. 2 and other experiments (Qin et al., 2023; Zhang et al., 2023).

3.2.2 Twin-twin plane

We can describe the compatible plane between two different twins with the average deformation matrices $\mathbf{U}_{ij}$ and $\mathbf{U}_{kl}$ respectively:

$$\begin{cases} \mathbf{U}_{ij} = \lambda_{ij}\mathbf{U}_i + (1-\lambda_{ij})\,\mathbf{Q}_{ij}\mathbf{U}_j, & (6.) \\ \mathbf{U}_{kl} = \lambda_{kl}\mathbf{U}_k + (1-\lambda_{kl})\,\mathbf{Q}_{kl}\mathbf{U}_l, & (7.) \\ \mathbf{R}_{ijkl}\mathbf{U}_{kl} - \mathbf{U}_{ij} = \mathbf{b}_{ijkl} \otimes \widehat{\mathbf{m}}_{ijkl} & (8.) \end{cases}$$

where λ_{ij} and λ_{kl} are the volume fractions of the major component $\mathbf{U}_i$ and $\mathbf{U}_k$in the twin $\mathbf{U}_{ij}$ and $\mathbf{U}_{kl}$, respectively; $\mathbf{R}_{ijkl}$ is the rotation acting on $\mathbf{U}_{kl}$; the two vectors $\mathbf{b}_{ijkl}$ and $\widehat{\mathbf{m}}_{ijkl}$ denote the shear vector and the plane normal, respectively. The procedure for solving the compatible twin-twin plane Eqs. (6) ~ (8) is similar to that for the habit plane in Eqs. (3) and (4). However, the number of solutions for the compatible twin-twin plane is different from that of the habit plane. The habit plane has limited solutions whose twins' major component has a fixed volume fraction (≈ 2/3 for the present cubic-to-tetragonal transformation) as shown in in Fig. 3 and Table A2, while the twin-twin plane can have infinite solutions (with infinite possible values of the volume fractions λ_{ij} and λ_{kl}). A simple example is the domain wall OC in Fig. 2(b), separating the two domains (twins) which have different volume fractions of the variants M_1 and M_3. If considering only the compatibility between these two twins, without taking into account the constraints from other domains (such as the domains of austenite and twin M_3M_2 in Fig. 2(b)), we can find infinite solutions: For example, when the normal $\widehat{\mathbf{m}}_{1331}$ of the domain wall OC has the same orientation as the twin boundary $\widehat{\mathbf{n}}_{\mathbf{13}}$ (also $\widehat{\mathbf{n}}_{\mathbf{31}}$), the volume fractions λ_{ij} and λ_{kl} (here the volume fractions of the twins' major components λ_{13} and λ_{31}) can be any value between 0.5 and 1. But, according

to current experiment (Fig. 2) and other experiments on the same material (Ni-Mn-Ga) in (Qin et al., 2023; Zhang et al., 2023), only a limited number of solutions (the twins with certain volume fractions) can be observed in the multiple-domain coexistence (such X-interface in (Qin et al., 2023) and the five-domain coexistence in Fig. 2). Therefore, we need to consider not only the compatibility of each domain wall, but also the global compatibility (the inter-constraints of the co-existing multiple domains) as in the following.

3.3 Global compatibility

In this section, we mainly follow the spirit of (Balandraud and Zanzotto, 2007; Balandraud et al., 2010) to characterize the inter-constraints of the multiple domains. First, taking the austenite as reference, we determine the deformation matrices (deformation gradients) of the twins M_3M_2 and M_1M_3 forming the habit planes OB and OD respectively. As discussed in Sections 3.1 and 3.2, the compatibility equations for these habit planes can be formulated.

For habit plane OB with twin M_3M_2:

$$\begin{cases} \mathbf{Q}_{32}\mathbf{U}_2 - \mathbf{U}_3 = \mathbf{a}_{32} \otimes \hat{\mathbf{n}}_{32} & (9.) \\ \mathbf{U}_{32} = \lambda_{32}\mathbf{U}_3 + (1-\lambda_{32})\,\mathbf{Q}_{32}\mathbf{U}_2, & (10.) \\ \mathbf{F}_{32} - \mathbf{I} = \mathbf{b}_{32} \otimes \hat{\mathbf{m}}_{32} & (11.) \end{cases}$$

where $\mathbf{F}_{32} = \mathbf{R}_{32}\mathbf{U}_{32}$ (with $\mathbf{R}_{32}$ being the rotation matrix acting on $\mathbf{U}_{32}$) and λ_{32} is the volume fraction of the variants $\mathbf{U}_3$ in the twin $\mathbf{U}_{32}$.

For habit plane OD with twin M_1M_3:

$$\begin{cases} \mathbf{Q}_{13}\mathbf{U}_3 - \mathbf{U}_1 = \mathbf{a}_{13} \otimes \hat{\mathbf{n}}_{13} & (12.) \\ \mathbf{U}_{13} = \lambda_{13}\mathbf{U}_1 + (1-\lambda_{13})\,\mathbf{Q}_{13}\mathbf{U}_3, & (13.) \\ \mathbf{F}_{13} - \mathbf{I} = \mathbf{b}_{13} \otimes \hat{\mathbf{m}}_{13} & (14.) \end{cases}$$

where $\mathbf{F}_{13} = \mathbf{R}_{13}\mathbf{U}_{13}$ (with $\mathbf{R}_{13}$ being the rotation matrix acting on $\mathbf{U}_{13}$) and $\lambda_{13}$is the volume fraction of the variants $\mathbf{U}_1$ in the twin $\mathbf{U}_{13}$.

After solving Eqs. (9) ~ (14), we have four solutions for each of the two deformation matrices $\mathbf{F}_{32}$ and $\mathbf{F}_{13}$ with the volume fractions λ_{32} and λ_{13} equal to around 2/3, as shown in Table A2 (Appendix A) and Fig. 3. By comparison with the experimentally observed domain wall OD in Fig. 2(b), only 2 of the calculated matrices $\mathbf{F}_{13}$ with the proper habit-plane orientations ($\widehat{\mathbf{m}}_{13} \approx$ [1 1 0] or [-1 -1 0]) are consistent with the current observation (OD is around 45° to *x*-axis). Thus, we have obtained four solutions of $\mathbf{F}_{32}$ and two solutions of $\mathbf{F}_{13}$ that can describe the two domains (twins M_3M_2 and M_1M_3) with the observed habit planes (OB and OD lines in Fig. 2). But, both domains II and III (twins with the deformation matrices $\mathbf{F}_{32}$ and $\mathbf{F}_{13}$) are contacting with domain I (twin M_3M_1); their compatibility also needs to be verified.

Then, we study the compatible domain wall OA separating the twin M_3M_1 and the twin M_3M_2 (with deformation matrix $\mathbf{F}_{32}$ among the four possible solutions obtained above):

$$\begin{cases} \mathbf{Q}_{31}\mathbf{U}_1 - \mathbf{U}_3 = \mathbf{a}_{31} \otimes \widehat{\mathbf{n}}_{31} & (15.) \\ \mathbf{U}_{31} = \lambda_{31}\mathbf{U}_3 + (1-\lambda_{31})\,\mathbf{Q}_{31}\mathbf{U}_1, & (16.) \\ \mathbf{F}_{31} - \mathbf{F}_{32} = \mathbf{b}_{3231} \otimes \widehat{\mathbf{m}}_{3231} & (17.) \end{cases}$$

where $\mathbf{F}_{31} = \mathbf{R}_{3231}\mathbf{U}_{31}$ (with $\mathbf{R}_{3231}$ being the rotation matrix acting on $\mathbf{U}_{31}$) and λ_{31} is the volume fraction of the variants $\mathbf{U}_3$ in the twin $\mathbf{U}_{31}$. The solutions of $\mathbf{F}_{31}$ are shown in Table A3, among which, 8 solutions with the orientations ($\widehat{\mathbf{m}}_{3231} \approx$ [1 1 0] or [-1 -1 0]) agree with the observed domain wall OA in Fig. 2.

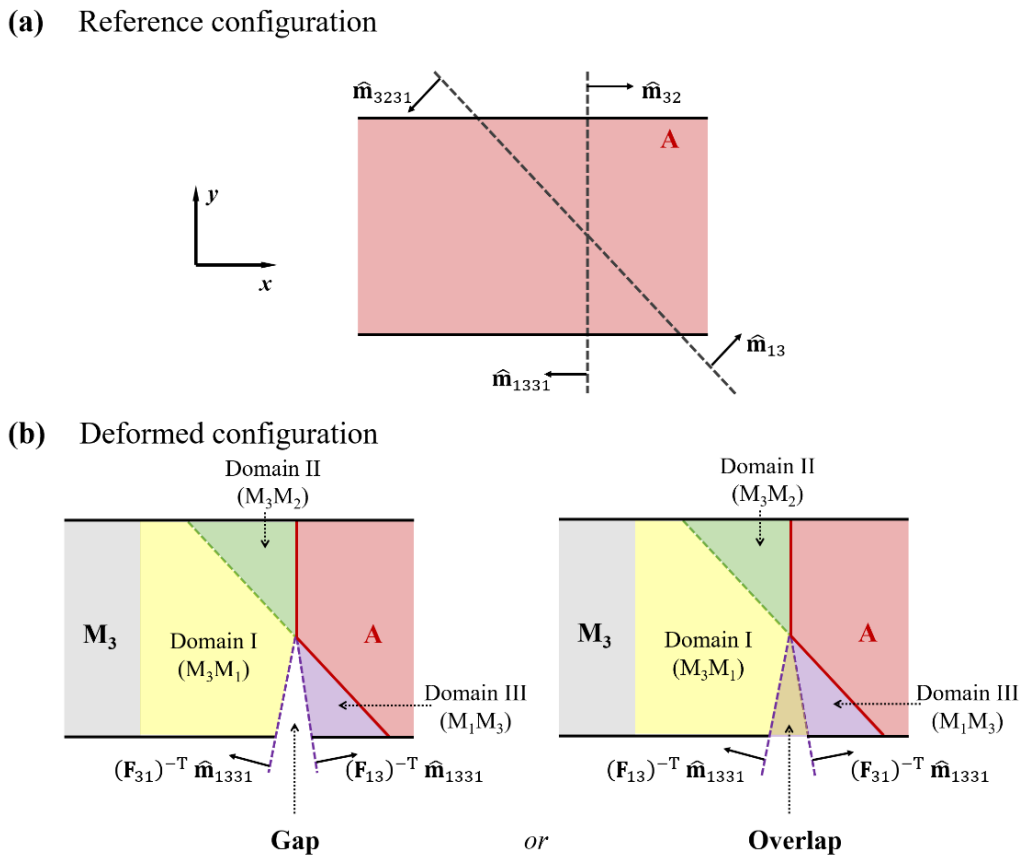

Fig. 4 (a) The multiple domains in the reference configuration (i.e., all are in the austenite state); (b) the multiple domains in the deformed configuration (i.e., the domains take different deformations that can generate a gap or overlap when the contact surface between the domains I and III is assumed to be released).

Finally, we check the compatibility between domains M_3M_1 and M_1M_3 (with the deformation matrices $\mathbf{F}_{13}$ and $\mathbf{F}_{31}$ obtained above) by the Hadamard jump condition:

$$\mathbf{F}_{31} - \mathbf{F}_{13} = \mathbf{b}_{1331} \otimes \hat{\mathbf{m}}_{1331} \tag{18.}$$

If there were solutions of the two vectors $\mathbf{b}_{1331}$ and $\hat{\mathbf{m}}_{1331}$ to satisfy Eq. (18), this multiple-domain coexistence would be perfectly compatible; otherwise, it would not be perfectly compatible or not compatible. For current material, there is no solution for the 16 combinations of

the matrices $\mathbf{F}_{13}$ (2 solutions) and $\mathbf{F}_{31}$ (8 solutions) obtained above that can satisfy Eq. (18). That means, after the transformation from the reference configuration (Fig. 4(a)) to the deformed configuration (Fig. 4(b)), there is a gap or overlap between domains M_3M_1 and M_1M_3. According to (Balandraud et al., 2010), an extra rotation matrix **R** can be added in Eq. (18) to achieve the "compatibility":

$$\mathbf{R}\,\mathbf{F}_{31} - \mathbf{F}_{13} = \mathbf{b}_{1331} \otimes \hat{\mathbf{m}}_{1331} \tag{19.}$$

With the solution to Eq. (19), we can estimate the degree (level) of the non-compatibility of the multiple-domain pattern. There are three different indicators in literature to estimate the non-compatibility magnitude as in the following:

- ***Rotation angle ψ***

After solving Eq. (19) with the matrices $\mathbf{F}_{13}$ and $\mathbf{F}_{31}$ (among the 16 combinations derived above), we have 32 solutions of $\hat{\mathbf{m}}_{1331}$ and the associated **R**. With the calculated rotation matrix **R**, we can define a rotation angle to characterize the non-compatibility:

$$\psi = \arccos\left(\frac{\mathrm{tr}\,\mathbf{R} - 1}{2}\right) \tag{20.}$$

The 32 values of ψ are shown in Fig. 6 and the detailed results are in Table A4 (Appendix A).

- ***Mismatch angle φ***

Based on the solution of Eq. (19), we have determined $\hat{\mathbf{m}}_{1331}$, which is the normal of the twin-twin plane separating the two domains M_3M_1 and M_1M_3 in the reference configuration. The magnitude of the gap or overlap between the two domains can be estimated by the mismatch angle φ defined in Eq. (21) and schematically plotted in Fig. 4(b).

$$\varphi = \arccos\left(\frac{|\mathrm{n}_1 \cdot \mathrm{n}_2|}{|\mathrm{n}_1||\mathrm{n}_2|}\right) \tag{21.}$$

where $\mathrm{n}_1 = (\mathbf{F}_{13})^{-\mathrm{T}}\hat{\mathbf{m}}_{1331}$ and $\mathrm{n}_2 = (\mathbf{F}_{31})^{-\mathrm{T}}\hat{\mathbf{m}}_{1331}$ are the normals of the twin-twin plane in the deformed configuration calculated on each side of the contact surface. Values for φ are also summarized in Table A4 (Appendix A) and in Fig. 6. As noted in (Balandraud et al., 2010), similarities can be found between the current problem and that of a fracture problem. By

construction, the mismatch angle φ can be seen as the mode I aperture of a crack whereas rotation angle ψ provides a more general evaluation of the mismatch (involving potentially analogs of crack modes I, II, III). Thus, φ is always lower or equal to ψ. But, as for a fracture problem, the "mode I" like angle φ should be more important in terms of stress concentration.

- ***Non-coplanarity angle θ***

As mentioned by (Ruddock, 1994), the normals of the domain walls of the perfectly compatible multi-domain pattern must be coplanar; i.e., the four domain walls (habit planes and twin-twin planes) cross at a single line as in Fig. 5(a). However, for the current non-perfectly compatible case, the solution to Eq. (19) gives $\mathbf{R} \neq \mathbf{I}$ (i.e., Eq. (18) has no solution); in addition, the normals of the domain walls may not be coplanar. According to (Seiner et al., 2009), the non-coplanarity in the reference configuration can be quantified by an angle θ in Eq. (22) and described schematically in Fig. 5(b).

$$\theta = |\arcsin(\hat{\mathbf{v}} \wedge \hat{\mathbf{w}})| \tag{22.}$$

where $\hat{\mathbf{v}} = \hat{\mathbf{m}}_{32} \wedge \hat{\mathbf{m}}_{\mathbf{13}}$ represents the intersecting line of the two habit planes and $\hat{\mathbf{w}} = \hat{\mathbf{m}}_{3231} \wedge \hat{\mathbf{m}}_{1331}$ represents the intersecting line of the two twin-twin planes.

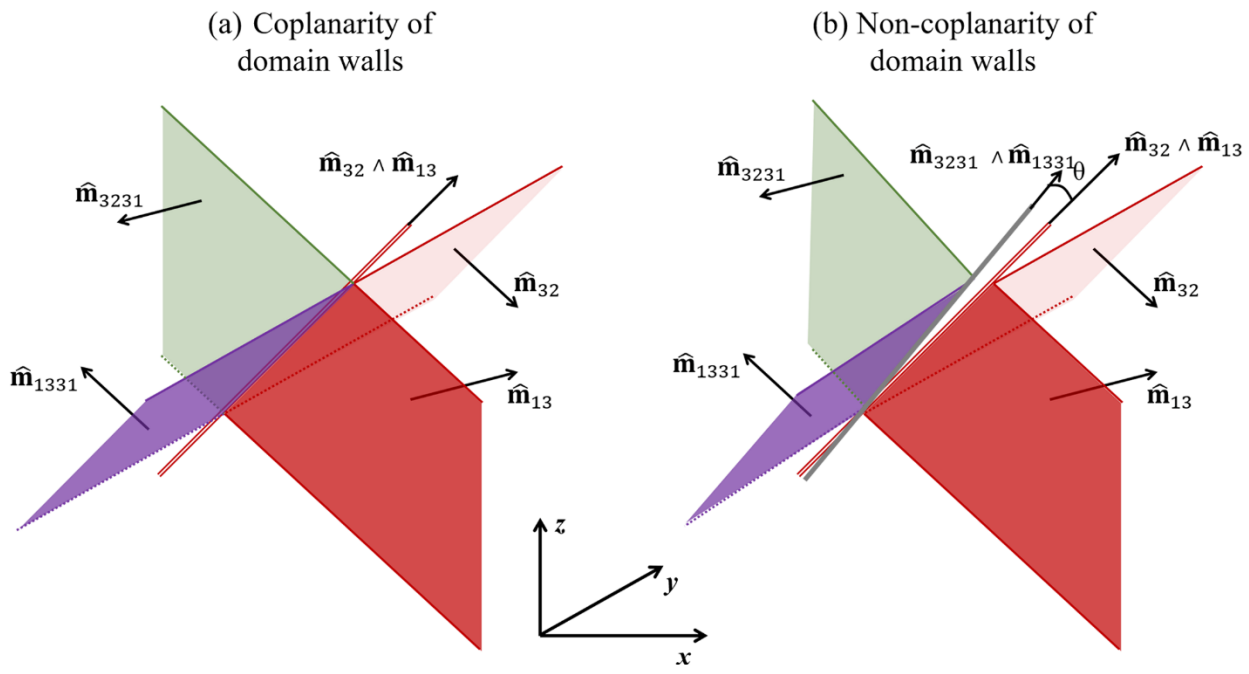

Fig. 5 (a) The perfect coplanarity of the unit normal vectors of the four domain walls; (b) The angle θ characterizing the case of a non-perfect coplanarity.

The calculated ψ, φ, and θ angles for the 32 solutions to Eq. (19) are plotted in Fig. 6 (sorted by the rotation angle ψ). The detailed results can be found in Appendix A where Table A4 lists the deformation matrices, the normals of twin-twin planes and habit planes, etc. It is seen in Fig. 6 that the 32 cases can be divided into two groups: (i) slightly non-compatible cases 1 ~ 16 where θ < 10°, ψ and φ are less than 0.25°; (ii) strongly non-compatible cases 17 ~ 32 where θ > 60°, ψ and φ are larger than 2.3°. Although the 32 cases can provide the traces of the domain walls (OA, OB, OC, and OD) agreeing with the experimental observation, only the cases of group (i) with slightly non-compatibility are possible to describe the equilibrium (or near-equilibrium) three-dimensional interfacial structure as shown in Fig. 7, where we plot the four optimal cases: cases 1 and 2 with ψ = 0.0542°, φ = 0.0555°, and θ = 0.6922°; cases 3 and 4 with ψ = 0.0606°, φ = 0.0612°, and θ = 0.5111°. The values of the indicator θ for the four optimal cases are smaller than 2.5° of the X-interface of (Seiner et al., 2009), and their ψ and φ values are smaller than 0.32° of the wedge pattern of (Balandraud and Zanzotto, 2007). That means, the observed five-domain pattern in Fig.

2 can be considered as near perfectly-compatible (causing only a little elastic strain), and can appear without a large driving force.

In fact, the previous study (Qin et al., 2023) on the same material (Ni-Mn-Ga) also demonstrated the formation of the four-domain structure (X-interface), whose non-compatibility indicators are calculated by similar procedures (details in Appendix B). The result shows that the X-interface in (Qin et al., 2023) can also have small values of the non-compatibility indicators: ψ (0.1238°), φ (0.1244°), and θ (0.3919°), which are close to the values of the four optimal cases of the five-domain interface in Fig. 7. That means, both the X-interface (four-domain coexistence in (Qin et al., 2023)) and five-domain coexistence in the current experiment (Fig. 2) can have similarly small values of the indicators (angles). Therefore, all the patterns of the multiple-domain coexistence (three-domain, four-domain, and five-domain) can be observed in the single crystal Ni-Mn-Ga in the current experiment and previous experiments (Qin et al., 2023; Zhang et al., 2023). Which pattern will finally win out might depend on the loading path, the material's initial state, and internal defects. The effects of these factors are studied in the following sub-section.

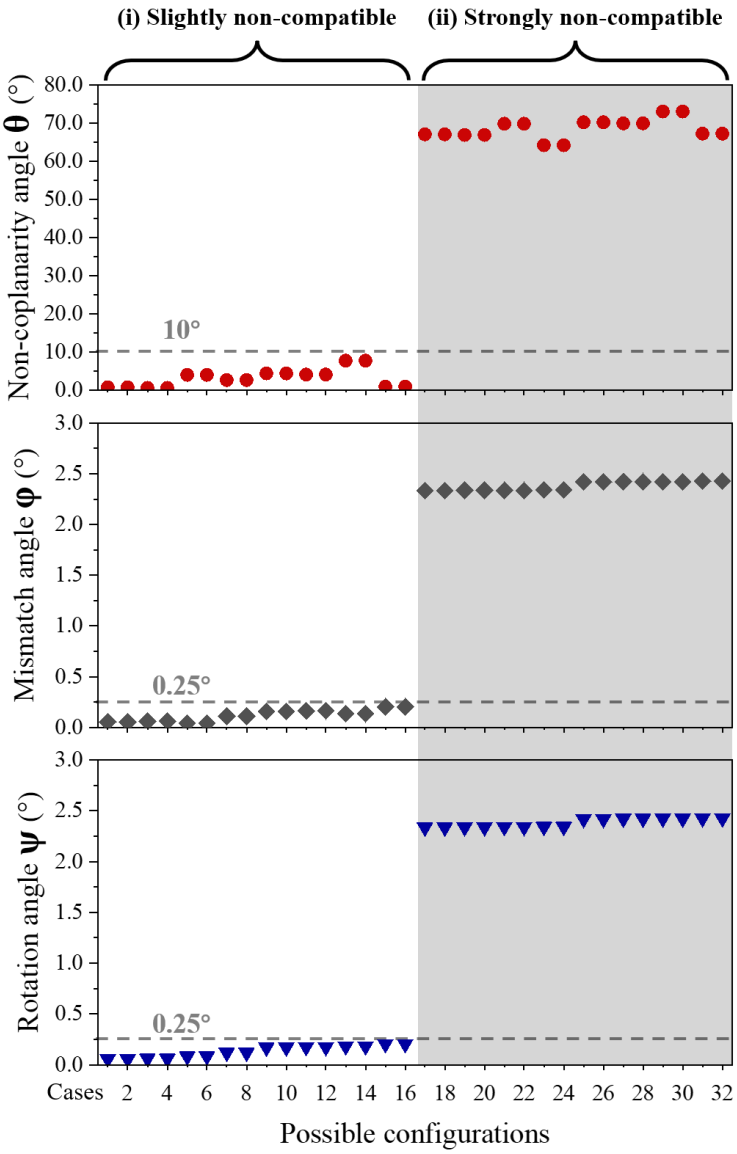

Fig. 6 The calculated non-coplanarity angle θ, mismatch angle φ, and rotation angle ψ (in degree) of the 32 cases capable to describe the experimentally observed domain walls on the specimen's top surface (*x*-*y* plane) in Fig. 2.

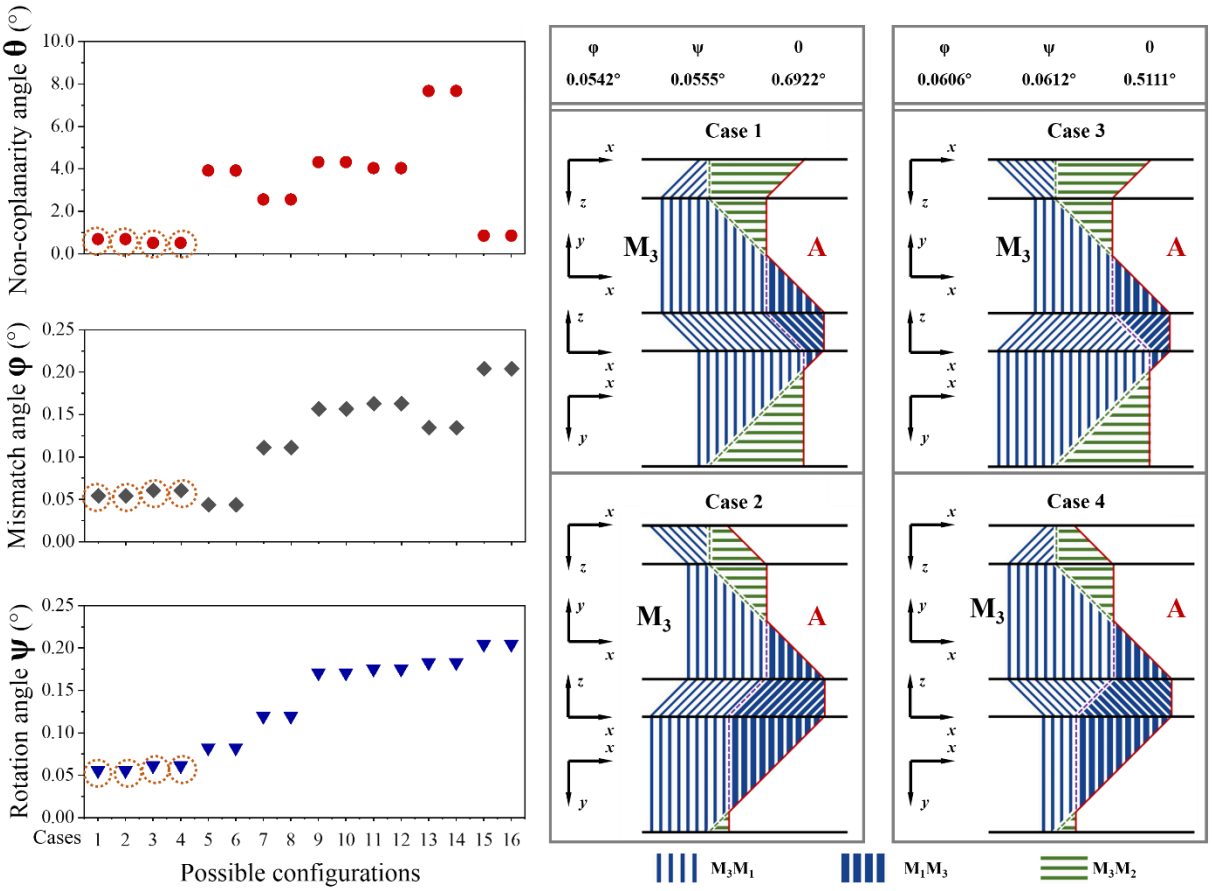

Fig. 7 The four optimal cases of the interfacial structures can have the same traces of the domain walls on the *x*-*y* plane (specimen's top surface) as in the experimental observation. The predicted traces on the other surfaces of the specimen need to be verified in future experiments.

3.4 Reason for five-domain formation

As mentioned in Section 2, the specimen's initial state is the single martensite variant M_3 whose short axis is along the specimen's thickness direction (*z*-direction), while the heating at the specimen's right end generates a thermal gradient along the *x*-direction ($\nabla T \,//\, x$) to drive the phase transformation from M_3 to the austenite via the propagation of a diffuse austenite-martensite interface as shown in Fig. 8. Based on the simple compatibility analysis results in Fig. 3, there are six possible twins to form habit planes. Considering the thermal loading ($\nabla T \,//\, x$) to drive the phase transformation, the habit planes should not be parallel to the *x*-direction. That is to say, only

four cases (the cases (a), (c), (e) and (f)) are possible. Because the initial state is M_3, the twins in the diffuse interfacial zone should include M_3. So, there are three possible twins (M_1M_3, M_2M_3 and M_3M_2 with ratio of ≈ 2:1) which can form the diffuse interfacial zone simultaneously connecting the austenite and M_3, leading to the three possible 3-domain configurations, namely (c), (e) and (f) in Fig. 8.

It should be noted that the three possible twins can connect to the single crystal M_3 by different kinds of domain walls. The twin M_1M_3 of the case (c) can connect to M_3 directly by their twinning boundary (twinning plane), while the twins M_2M_3 and M_3M_2 of the cases (e) and (f) connect to M_3 via a special domain wall—a needle transitional zone making the volume fraction of M_3 change from 100% ($f_{M_3} = 1$ in single variant M_3) to 33% (f_{M_3} = 1/3 in twin M_2M_3) and 67% (f_{M_3} = 2/3 in twin M_3M_2), respectively. An example of the needle pattern is shown in Fig. 8. More detailed experiments and discussion on the needle patterns can be found in (Zhang et al., 2018a; Zhang et al., 2023). As the needle-like domain wall would cost energy, it is expected that the M_3M_2 of case (f) is better than the M_2M_3 of case (e) in connection to the single variant M_3, considering that the volume fraction difference between the M_3M_2 and M_3, Δf_{M_3} = 1–2/3 = 1/3, is less than that between the M_2M_3 and M_3 (where Δf_{M_3} = 1–1/3 = 2/3). That might explain the experimental observation in literature (Qin et al., 2023; Zhang et al., 2023): the case (f) of the three-domain configuration has been observed, while the case (e) did not appear. This means that the most likely three-domain configurations are only the cases (c) and (f).

Among the two most possible three-domain configurations, which one would win out depends on the fluctuation/nucleation at the beginning of the phase transformation, and on the defects (such as residual martensite variants M_1 or/and M_2 in the specimen). Anyway, if both M_1 and M_2 participate in the phase transformation, the cases (c) and (f) in Fig. 8 can be generated simultaneously to form more complicated interfacial zones, such as the four-domain configurations in Fig. 9, where the domain of single variant M_3 is connected to the twin M_1M_3 (the configuration (i)) or M_3M_2 (the configuration (ii)), or both (the configuration (iii)). It is seen that, in the configurations (i) and (ii), the two twins M_1M_3 and M_3M_2 would need to contact to each other. But these are not compatible, as shown in the following analysis.

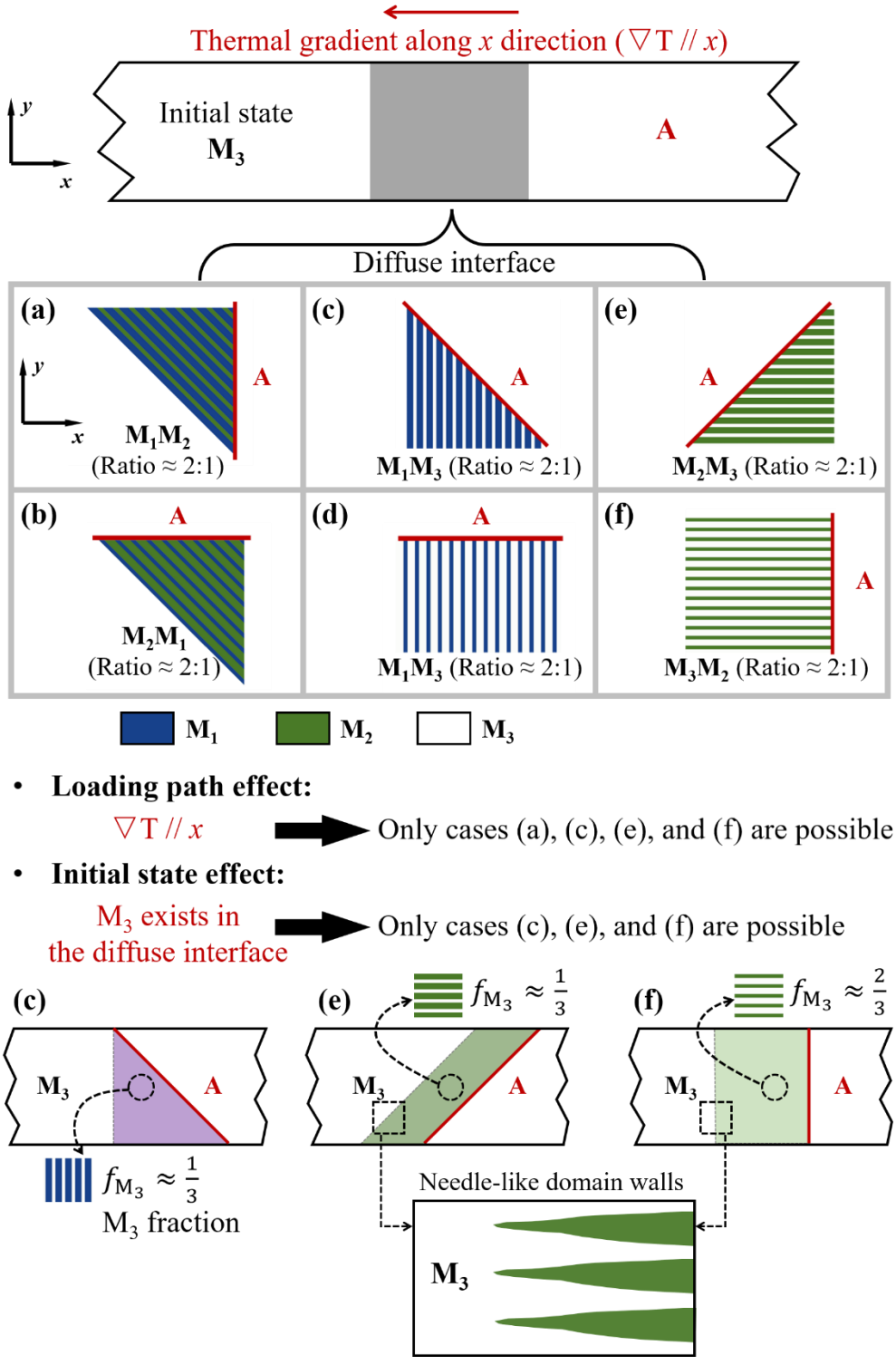

Fig. 8 The possible three-domain configurations from the material initial state M_3 subjected to a thermal gradient along the specimen's longitudinal direction (*x*-direction).

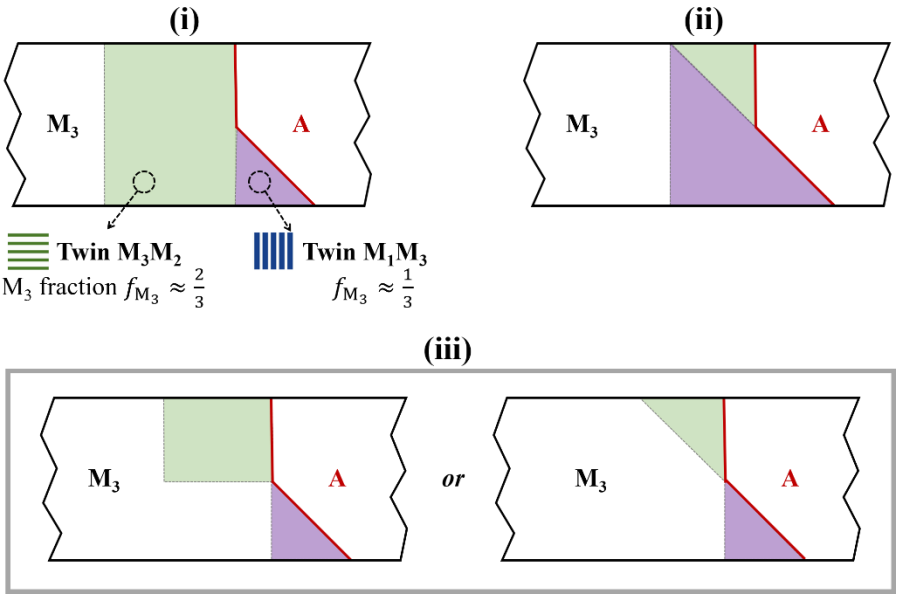

Fig. 9 The four-domain configurations. The configurations (i) and (ii) are not possible due to the incompatibility between the twins M_3M_2 and M_1M_3. The configuration (iii) is possible, but not yet observed experimentally.

Based on Eq. (4), the average characteristic deformation matrix for the twins M_1M_3 and M_3M_2 are denoted as $\mathbf{U}_{13}$ and $\mathbf{U}_{32}$, respectively, which can be approximately expressed as:

$$\mathbf{U}_{13} = \frac{2}{3}\begin{pmatrix}\alpha & 0 & 0\\ 0 & \beta & 0\\ 0 & 0 & \beta\end{pmatrix} + \frac{1}{3}\begin{pmatrix}\beta & 0 & 0\\ 0 & \beta & 0\\ 0 & 0 & \alpha\end{pmatrix} = \frac{1}{3}\begin{pmatrix}2\alpha+\beta & 0 & 0\\ 0 & \beta & 0\\ 0 & 0 & \alpha+2\beta\end{pmatrix} \approx \begin{pmatrix}0.98 & 0 & 0\\ 0 & 1.02 & 0\\ 0 & 0 & 1\end{pmatrix} \tag{23a}$$

$$\mathbf{U}_{32} = \frac{2}{3}\begin{pmatrix}\beta & 0 & 0\\ 0 & \beta & 0\\ 0 & 0 & \alpha\end{pmatrix} + \frac{1}{3}\begin{pmatrix}\beta & 0 & 0\\ 0 & \alpha & 0\\ 0 & 0 & \beta\end{pmatrix} = \frac{1}{3}\begin{pmatrix}\beta & 0 & 0\\ 0 & \alpha+2\beta & 0\\ 0 & 0 & 2\alpha+\beta\end{pmatrix} \approx \begin{pmatrix}1.02 & 0 & 0\\ 0 & 1 & 0\\ 0 & 0 & 0.98\end{pmatrix} \tag{23b}$$

with $\alpha \approx 0.96$ and $\beta \approx 1.02$. It should be noted that the rotation Q in Eq. (4) is ignored here for the following simplified analysis. According to the deformation matrices in Eq. (23) and the compatibility analysis in Appendix A and (Bhattacharya, 2003), these two twins are not compatible with each other. So, the configurations (i) and (ii) in Fig 9 are not energetic preferable. By contrast,

the configuration (iii) is possible (like the four-domain configuration of the λ-interface in Fig. 1); however, it has not been observed experimentally in current material.

Another choice for the pattern formation is the five-domain configuration as shown in Fig. 10 where a "buffering" zone separates the three domains: the domains of single variant M_3, and the twins M_1M_3 and M_3M_2. That means, the buffering zone needs to be compatible simultaneously with the three domains. If the buffering zone is assumed as a twin including M_3 as a component (because of the initial state M_3), there are two possible compositions for the buffering zone: M_3—M_1 (Fig. 10(a)) and M_3—M_2 (Fig. 10(b)), whose volume fractions of M_3 denoted as f_{M3} can be determined theoretically in the following sub-sections.

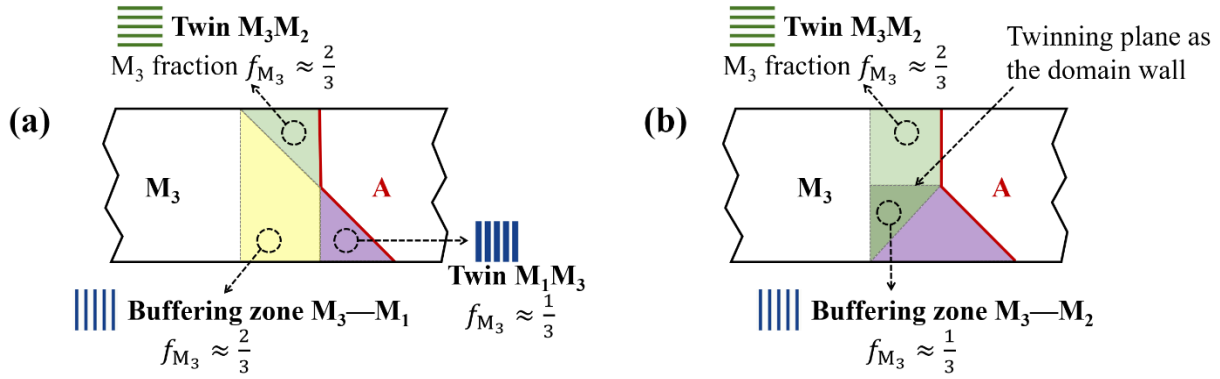

Fig. 10 The possible five-domain configurations: (a) the buffering zone M_3—M_1 with the volume fraction $f_{M_3} = 2/3$ can be compatible with all its neighboring domains, which agrees with the current experimental observation in Fig. 2; (b) the buffering zone M_3—M_2 with volume fraction $f_{M_3} = 1/3$ can be compatible with all its neighboring domains, but it was not observed experimentally.

3.4.1 Buffering zone M_3—M_1

The deformation matrices of the single variant M_3 and the buffering zone M_3—M_1 are denoted as $\mathbf{U}_3$ and $\mathbf{U}_{M_3-M_1}$, respectively.

$$\mathbf{U}_3 = \begin{pmatrix} \beta & 0 & 0 \\ 0 & \beta & 0 \\ 0 & 0 & \alpha \end{pmatrix} \tag{24a}$$

$$\mathbf{U}_{M_3-M_1} = f_{M_3}\begin{pmatrix} \beta & 0 & 0 \\ 0 & \beta & 0 \\ 0 & 0 & \alpha \end{pmatrix} + (1 - f_{M_3})\begin{pmatrix} \alpha & 0 & 0 \\ 0 & \beta & 0 \\ 0 & 0 & \beta \end{pmatrix}$$
$$= \begin{pmatrix} \alpha(1 - f_{M_3}) + \beta f_{M_3} & 0 & 0 \\ 0 & \beta & 0 \\ 0 & 0 & \alpha f_{M_3} + \beta(1 - f_{M_3}) \end{pmatrix} \tag{24b}$$

It is seen from Eqs. (23a), (24a) and (24b) that all the deformation matrices $\mathbf{U}_{13}$, $\mathbf{U}_3$ and $\mathbf{U}_{M3-M1}$ have β as the second diagonal component. That means, these domains can be easily compatible to each other. In fact, their compatible domain walls are just their twining boundaries (twining planes) as shown in Fig. 2.

In addition, the buffering zone M_3—M_1 needs also compatible with the twin M_3M_2. That means, one of the diagonal components in their deformation matrices (Eqs. (23(b) and (24b)) must be equal to each other.

$$\alpha(1 - f_{M_3}) + \beta f_{M_3} = \frac{1}{3}\beta \tag{25a}$$

$$\text{or} \quad \frac{1}{3}(\alpha + 2\beta) = \beta \tag{25b}$$

$$\text{or} \quad \alpha f_{M_3} + \beta(1 - f_{M_3}) = \frac{2\alpha+\beta}{3} \tag{25c}$$

Eq. (25b) is obviously impossible as $\alpha \neq \beta$ ($\alpha \approx 0.96$ and $\beta \approx 1.02$). Eq. (25a) leads to $f_{M_3} = \frac{\frac{1}{3}\beta-\alpha}{\beta-\alpha} < 0$. So, only Eq. (25c) gives the reasonable prediction $f_{M_3} = 2/3$ which agrees with the current experiments in Fig. 2. That means, the twin buffering zone M_3—M_1 of the five-domain pattern in Fig. 10(a) must have the volume fraction $f_{M_3} = 2/3$ to be compatible to all its neighboring domains.

3.4.2 Buffering zone M_3—M_2

Similarly, the deformation matrix of the buffering zone M_3—M_2 is denoted as $\mathbf{U}_{M_3-M_2}$,

$$\mathbf{U}_{M_3-M_2} = f_{M_3}\begin{pmatrix}\beta & 0 & 0\\ 0 & \beta & 0\\ 0 & 0 & \alpha\end{pmatrix} + (1-f_{M_3})\begin{pmatrix}\beta & 0 & 0\\ 0 & \alpha & 0\\ 0 & 0 & \beta\end{pmatrix}$$
$$= \begin{pmatrix}\beta & 0 & 0\\ 0 & \beta f_{M_3} + \alpha(1-f_{M_3}) & 0\\ 0 & 0 & \alpha f_{M_3} + \beta(1-f_{M_3})\end{pmatrix} \quad (26)$$

For the compatibility between the buffering zone M_3—M_2 and the twin M_1M_3, one of the diagonal components in their deformation matrices, Eqs. (26) and 23(a), must be equal to each other.

$$\tfrac{1}{3}(2\alpha+\beta) = \beta \quad (27a)$$

$$\text{or} \quad \beta f_{M_3} + \alpha(1-f_{M_3}) = \tfrac{1}{3}\beta \quad (27b)$$

$$\text{or} \quad \alpha f_{M_3} + \beta(1-f_{M_3}) = \tfrac{\alpha+2\beta}{3} \quad (27c)$$

Similarly, Eq. (27a) is obviously impossible as $\alpha \neq \beta$ ($\alpha \approx 0.96$ and $\beta \approx 1.02$). Eq. (27b) leads to $f_{M_3} = \frac{\frac{1}{3}\beta-\alpha}{\beta-\alpha} < 0$. So, only Eq. (27c) gives prediction $f_{M_3} = 1/3$.

In addition, the buffering zone M_3—M_2 and the twin M_3M_2 need compatible with each other, which is easy via their twinning boundary (twinning planes). However, their twinning plane is parallel to the *x*-direction as shown in Fig. 10(b). That means, such buffering zone does not really separate the single domain M_3 from the twin M_3M_2 (domain II in Fig. 2). As a result, this explains why the five-domain configuration in Fig. 10(b) was not observed experimentally.

In summary, considering the loading path (thermal gradient along *x*-direction) and the material initial state (M_3), there are only a few possible three-domain, four-domain, and five-

domain configurations. Which one would appear depends on the fluctuation/defects during the phase transformation. Particularly, if both M_1 and M_2 participate in the phase transformation, the most possible configuration is the 5-domain configuration in Fig. 10(a), which agrees with the current experimental observation (Fig. 2).

4. Discussions

Among many external loading parameters and material internal factors influencing the domain-pattern formation, the interface kinetics (driving force or interface velocity) and the initial state/defects are mostly mentioned in literature. For example, the simple two-domain coexistence with perfect compatibility between austenite and a martensite variant implies little elastic energy and small hysteresis (low energy dissipation) (Cui et al., 2006; Chen et al., 2013; Gu et al., 2018); by contrast, the relatively complex *non-perfectly compatible* domain patterns such as wedges and X-interfaces are expected to appear with larger driving force (e.g., higher thermal gradient) (Ruddock, 1994; Balandraud and Zanzotto, 2007; Stupkiewicz et al., 2007; Seiner et al., 2008; Balandraud et al., 2010; Petryk and Stupkiewicz, 2010; Stupkiewicz et al., 2021). In normal interface kinetics, larger driving force leads to faster interface propagation (Abeyaratne and Knowles, 1991; Faran and Shilo, 2011, 2015). Then, there might be a relation between the interfacial structure and the interface propagation velocity. However, up to now, we have only a few data: the velocity of the five-domain interface in current experiment is around 280 μm /s (see the movies in supplementary material); the four-domain interface (X-interface) propagates at around 170 μm/s in (Qin et al., 2023); and the speed of the three-domain interface is in the range of 280 ~ 520 μm/s (Qin et al., 2023; Zhang et al., 2023). A clear relation between the interfacial structure and speed is not yet established. The reason might be that the interface kinetics depends on the energy barriers caused by not only the elastic energy (due to the interface non-compatibility), but also the material's initial state or/and defects/imperfections (Chang and Read, 1951; Zreihan et al., 2015). The initial-state effect on the interfacial structure was clearly demonstrated in (Qin et al., 2023) while material imperfections such as the residual stress and the inhomogeneous chemical compositions were discussed in (Chang and Read, 1951; Ruddock, 1994). Once a certain domain pattern was nucleated due to the defects or the initial state, it would continue during the interface propagation because most of the domain patterns are meta-stable (near local energy

minimizer). That means, various domain patterns might appear randomly, depending on the interface nucleation or the barriers/obstacles the propagating interface encounter.

Strictly speaking, the five coexisting domains emphasized in this paper just show the meso-scale features of a macroscopic diffuse austenite-martensite interface in the Ni-Mn-Ga magnetic SMA. Within each domain, there are many sub-domains such as the twin laminate (Fig. 2), the magnetic domains (in the ferromagnetic austenite and martensite of the current material with a Curie temperature around 100 ℃) (Kiefer and Lagoudas, 2005; Peng et al., 2015; Qin et al., 2023), the so-called "AB twin", and "modulation twin" (if the slightly monoclinic deformation in the martensite takes effect (Straka et al., 2011; Chulist et al., 2013; Heczko et al., 2013; Pascan et al., 2015; Qin et al., 2023)). The interactions between these sub-domains can generate much more complicated patterns including numerous microscopic domain walls, whose interfacial energy is ignored in usual compatibility analysis (Ruddock, 1994). Alternatively, the effects of these sub-domains and microscopic domain walls might be taken into account in macroscopic continuum models by multi-scale analysis such as (Stupkiewicz et al., 2021). Even though the global continuum model might not be simple (e.g., with the softening stress-strain curve and non-convex energy), the macroscopic process, the single-interface propagation in a SMA single crystal, is very simple, compared with the phase transformation in polycrystals.

In the grains of a polycrystalline SMA, the nucleation and propagation of *multiple* interfaces would take place. Moreover, due to the constraints of the grain boundaries and the grain-grain interactions, the interface propagation would encounter various resistant forces generating complex domain patterns, most of which are far from compatibility; i.e., lots of elastic energy is stored in the domain patterns (Salzbrenner and Cohen, 1979; Christian, 1982; Wollants et al., 1993; Levitas et al., 2010; Petryk and Stupkiewicz, 2010). For example, the diamond pattern (one of the self-accommodating martensite microstructures generated within the sea of austenite) is not a compatible configuration based on the analysis of (Hane and Shield, 1998). The large elastic energy stored in the grains during phase transformation would cause large energy dissipation (hysteresis) because the energy storage and release do not occur smoothly, but happen suddenly (unstable process) (He, 2023). That might be the reason for the empirical rule: the hysteresis of polycrystalline SMA is usually higher than that of single crystals. In the current study on single crystal, although the interfacial structure includes multiple domains, the compatibility analysis

demonstrates that these domain patterns are near perfectly compatible with small elastic energy so that the hysteresis is not large in the single crystal SMA.

5. Summary and conclusions:

The experimental observation on the five-domain interfacial structure is reported and accompanied by a compatibility analysis, comparing the non-compatibility between the new pattern and the previously reported four-domain pattern (X-interface), with three different indicators to characterize the degree of the non-compatibility. Moreover, the effects of the thermal loading path and the material initial state have been studied. Some conclusions can be drawn:

1. The elasticity due to the non-compatibility of the complex domain patterns in the interfacial structure would generate energy barrier for the phase transformation. In a clean single crystal (with little defect), the perfectly compatible patterns (such as the three-domain pattern with planar interface in Fig. 1(b)) would be generated more easily than the complex patterns such as the four-domain and five-domain patterns (which are not perfectly compatible).
2. The non-compatibility indicators show that both the present five-domain pattern and the four-domain pattern (X-interface) in the single crystals are very near the perfect compatibility, implying that they would cause only small elastic energy and can appear without large driving forces.
3. The compatibility analysis predicts several near-perfectly-compatible configurations of the five-domain interfaces whose formation/nucleation might depend on the loading condition, the material's initial state and defects.

Declaration of Competing Interest

The authors declare that they have no known competing financial interests or personal relationships that could have appeared to influence the work reported in this paper.

Acknowledgements

Chengguan Zhang would like to acknowledge China Scholarship Council (CSC) for the financial support (NO. 202006890005).

Appendix A: ***Compatibility solution procedures***

Following the method in (Ball and James, 1992; James and Hane, 2000; Bhattacharya, 2003; Balandraud et al., 2010; Zhang et al., 2018a), if $\mathbf{F_I}$ and $\mathbf{F_{II}}$ were defined as a pair of homogenous deformation gradients and a planar interface with normal $\hat{\mathbf{n}}$ existing between the two parts, the perfectly compatible interface plane can be achieved when the Hadamard condition of kinematic compatibility holds:

$$\mathbf{R}\quad \mathbf{F_I} - \mathbf{F_{II}} = \mathbf{a}\quad \otimes \hat{\mathbf{n}} \tag{A.1}$$

where $\mathbf{R}$ is the rotation, $\mathbf{a}$ is the shear vector, $\hat{\mathbf{n}}$ is the unit normal of the interface in the reference (undeformed) configuration. A sufficient and necessary condition for Eq. (A.1) to have solutions is that the matrix $\mathrm{C} = \mathbf{F_{II}}^{-\mathrm{T}}\,\mathbf{F_I}^{\mathrm{T}}\,\mathbf{F_I}\,\mathbf{F_{II}}^{-1}$ has ordered eigenvalues $\mu_1 \le \mu_2 = 1 \le \mu_3$, and the solutions to Eq. (A.1) can be given in pair as follows:

$$\begin{cases} \hat{\mathbf{n}}^{\pm} = \frac{\sqrt{\mu_3}-\sqrt{\mu_1}}{\rho\sqrt{\mu_3-\mu_1}}\left(-\sqrt{1-\mu_1}\,\mathbf{F_{II}^{\mathrm{T}}}\,\mathbf{e}_1 + k\sqrt{\mu_3-1}\,\mathbf{F_{II}^{\mathrm{T}}}\,\mathbf{e}_3\right) \\ \mathbf{a}^{\pm} = \frac{\rho}{\sqrt{\mu_3-\mu_1}}\left(\sqrt{\mu_3(1-\mu_1)}\,\mathbf{e}_1 + k\sqrt{\mu_1(\mu_3-1)}\,\mathbf{e}_3\right) \end{cases} \tag{A.2}$$

where ρ is a constant to make $\hat{\mathbf{n}}$ a unit vector, $\mathbf{e}_1$ and $\mathbf{e}_3$ are the eigenvectors corresponding to μ_1 and μ_3, respectively, and the notation '±' of $\hat{\mathbf{n}}$ and $\mathbf{a}$ is corresponding to $k = \pm 1$. Once $\hat{\mathbf{n}}$ and $\mathbf{a}$ are calculated, the rotation $\mathbf{R}$ can be obtained by substituting $\hat{\mathbf{n}}$ and $\mathbf{a}$ back to Eq. (A.1).

1. Twinning equations

By substituting the Bain matrices $\mathbf{U}_i$ and $\mathbf{U}_j$ (defined in Eq. (2)) into $\mathbf{F_I}$ and $\mathbf{F_{II}}$ in Eq. (A.1), we

can obtain the twinning equation:

$$\mathbf{Q}_{ij}\,\mathbf{U}_j \;-\; \mathbf{U}_{\mathrm{i}} \;=\; \mathbf{a}_{ij} \otimes \hat{\mathbf{n}}_{ij} \tag{A.3}$$

where $\mathbf{Q}_{ij}$ is the rotation acting on $\mathbf{U}_j$. Solving Eq. (A.3) with the different combinations of the three tetragonal martensite variants can give all the orientations of the compatible twin planes (twin boundaries), which are summarized in Table A1. The results indicate that the projection of the twinning plane between M_1 and M_2 on the *x*-*y* plane is 45° to the *x*-axis, while that of the twinning plane between M_1 and M_3 (M_3 and M_2) is vertical (parallel) to the *x*-axis as shown in Fig. 3.

Table A1 Solutions for twinning equations between martensite variants M_i and M_j.

	Normal of the twinning plane $\hat{\mathbf{n}}_{ij}$	Rotation acting on M*j* in M_iM_j Q_{ij}
M₁-M₂	$\hat{\mathbf{n}}_{12}^{+} = \frac{\sqrt{2}}{2}[1\ \ -1\ \ 0]$	$Q_{12}^{+} = \begin{pmatrix} 0.9983 & -0.0588 & 0 \\ 0.0588 & 0.9983 & 0 \\ 0 & 0 & 1 \end{pmatrix}$
	$\hat{\mathbf{n}}_{12}^{-} = \frac{\sqrt{2}}{2}[-1\ \ -1\ \ 0]$	$Q_{12}^{-} = \begin{pmatrix} 0.9983 & 0.0588 & 0 \\ -0.0588 & 0.9983 & 0 \\ 0 & 0 & 1 \end{pmatrix}$
M₂-M₁	$\hat{\mathbf{n}}_{21}^{+} = \frac{\sqrt{2}}{2}[-1\ \ 1\ \ 0]$	$Q_{21}^{+} = \begin{pmatrix} 0.9983 & 0.0588 & 0 \\ -0.0588 & 0.9983 & 0 \\ 0 & 0 & 1 \end{pmatrix}$
	$\hat{\mathbf{n}}_{21}^{-} = \frac{\sqrt{2}}{2}[-1\ \ -1\ \ 0]$	$Q_{21}^{-} = \begin{pmatrix} 0.9983 & -0.0588 & 0 \\ 0.0588 & 0.9983 & 0 \\ 0 & 0 & 1 \end{pmatrix}$
M₁-M₃	$\hat{\mathbf{n}}_{13}^{+} = \frac{\sqrt{2}}{2}[1\ \ 0\ \ -1]$	$Q_{13}^{+} = \begin{pmatrix} 0.9983 & 0 & -0.0588 \\ 0 & 1 & 0 \\ 0.0588 & 0 & 0.9983 \end{pmatrix}$
	$\hat{\mathbf{n}}_{13}^{-} = \frac{\sqrt{2}}{2}[-1\ \ 0\ \ -1]$	$Q_{13}^{-} = \begin{pmatrix} 0.9983 & 0 & 0.0588 \\ 0 & 1 & 0 \\ -0.0588 & 0 & 0.9983 \end{pmatrix}$
M₃-M₁	$\hat{\mathbf{n}}_{31}^{+} = \frac{\sqrt{2}}{2}[-1\ \ 0\ \ 1]$	$Q_{31}^{+} = \begin{pmatrix} 0.9983 & 0 & 0.0588 \\ 0 & 1 & 0 \\ -0.0588 & 0 & 0.9983 \end{pmatrix}$
	$\hat{\mathbf{n}}_{31}^{-} = \frac{\sqrt{2}}{2}[-1\ \ 0\ \ -1]$	$Q_{31}^{-} = \begin{pmatrix} 0.9983 & 0 & -0.0588 \\ 0 & 1 & 0 \\ 0.0588 & 0 & 0.9983 \end{pmatrix}$
M₂-M₃	$\hat{\mathbf{n}}_{23}^{+} = \frac{\sqrt{2}}{2}[0\ \ 1\ \ -1]$	$Q_{23}^{+} = \begin{pmatrix} 1 & 0 & 0 \\ 0 & 0.9983 & -0.0588 \\ 0 & 0.0588 & 0.9983 \end{pmatrix}$
	$\hat{\mathbf{n}}_{23}^{-} = \frac{\sqrt{2}}{2}[0\ \ -1\ \ -1]$	$Q_{23}^{-} = \begin{pmatrix} 1 & 0 & 0 \\ 0 & 0.9983 & 0.0588 \\ 0 & -0.0588 & 0.9983 \end{pmatrix}$
M₃-M₂	$\hat{\mathbf{n}}_{32}^{+} = \frac{\sqrt{2}}{2}[0\ \ -1\ \ 1]$	$Q_{32}^{+} = \begin{pmatrix} 1 & 0 & 0 \\ 0 & 0.9983 & 0.0588 \\ 0 & -0.0588 & 0.9983 \end{pmatrix}$
	$\hat{\mathbf{n}}_{32}^{-} = \frac{\sqrt{2}}{2}[0\ \ -1\ \ -1]$	$Q_{32}^{-} = \begin{pmatrix} 1 & 0 & 0 \\ 0 & 0.9983 & -0.0588 \\ 0 & 0.0588 & 0.9983 \end{pmatrix}$

2. Habit plane equations

In Eq. (A.1), when $\mathbf{F_{II}} = \mathbf{I}$ for austenite and $\mathbf{F_I} = \mathbf{U}_{ij} = \lambda_{ij}\mathbf{U}_i + (1-\lambda_{ij})\,\mathbf{Q}_{ij}\mathbf{U}_j$ for the deformation gradient of the twin M_iM_j (λ_{ij} is the volume fraction of the major component M_i in the twin), the compatibility condition of the austenite-twin interface can be expressed as:

$$\mathbf{R}_{ij}\,\mathbf{U}_{ij} - \mathbf{I} = \mathbf{b}_{ij} \otimes \widehat{\mathbf{m}}_{ij} \tag{A.4}$$

where $\mathbf{R}_{ij}$ is the rotation acting on $\mathbf{U}_{ij}$ and $\mathbf{F}_{ij} = \mathbf{R}_{ij}\,\mathbf{U}_{ij}$ describes the deformation gradient of the rotated twin M_iM_j. According to (Bhattacharya, 2003), the necessary and sufficient conditions for Eq. (A.4) are:

$$\begin{cases} \mathbf{a}_{ij} \cdot \mathbf{U}_i\,(\mathbf{U}_i^2 - 1)^{-1}\,\widehat{\mathbf{n}}_{ij} \le -2 \\ \mathrm{tr}(\mathbf{U}_i^2) - \det(\mathbf{U}_i^2) - 2 + \dfrac{|\mathbf{a}_{ij}|^2}{2\,\mathbf{a}_{ij}\cdot\mathbf{U}_i\,(\mathbf{U}_i^2-1)^{-1}\,\widehat{\mathbf{n}}_{ij}} \ge 0 \end{cases} \tag{A.5}$$

where $\mathbf{a}_{ij}$ and $\widehat{\mathbf{n}}_{ij}$ are solutions to Eq. (A.3). And there are two λ values that are given as:

$$\begin{cases} \lambda_{ij}^{\mathrm{I}} = \frac{1}{2}\left(1 - \sqrt{1 + \dfrac{2}{\mathbf{a}_{ij}\cdot\mathbf{U}_i\,(\mathbf{U}_i^2-1)^{-1}\,\widehat{\mathbf{n}}_{ij}}}\right) \\ \lambda_{ij}^{\mathrm{II}} = 1 - \lambda_{ij} \end{cases} \tag{A.6}$$

Two values can be obtained from Eq. (A.6): $\lambda_{ij} \approx 0.6823$ or 0.3177. The former value $\lambda_{ij} \approx 0.6823$ is selected because λ_{ij} is defined as the major volume fraction in the current study. The solutions to Eq. (A.4) are listed in Table A2, where we can see that, for each twin M_iM_j of the habit plane, there are four solutions (a) ~ (d) of the habit plane unit normal $\widehat{\mathbf{m}}_{ij}$, the deformation gradient $\mathbf{F}_{ij}$, etc. The projections of the habit planes onto the *x*-*y* plane are plotted in Fig. 3, which help identify the composition of the twinning structures in the experimental observation.

Table A2 Compatible planes (habit planes) between austenite phase and martensite twins. The solutions marked in grey are consistent with the current experimental observation (giving similar traces (or projections) of the habit planes and twinning planes on the specimen's *x*-*y* plane).

Twin M_iM_j	$\mathbf{Q}_{ij}$ acting on Mj	λ_{ij}	Normal of the habit plane $\hat{\mathbf{m}}_{ij}$	Rotation acting on M_iM_j R_{ij}	Deformation gradient $\mathbf{F}_{ij}$
M_1M_2	Q_{12}^{+}	0.6823	$\hat{\mathbf{m}}_{\mathbf{12}}$(a) [0.7245 -0.0253 0.6888]	$\mathbf{R}_{12}$(a) $\begin{pmatrix} 0.9996 & 0.0187 & -0.0200 \\ -0.0187 & 0.9998 & 0.0007 \\ 0.0200 & -0.0003 & 0.9998 \end{pmatrix}$	$\mathbf{F}_{12}$(a)
			$\hat{\mathbf{m}}_{\mathbf{12}}$(b) [0.7245 -0.0253 -0.6888]	$\mathbf{R}_{12}$ (b) $\begin{pmatrix} 0.9996 & 0.0187 & 0.0200 \\ -0.0187 & 0.9998 & -0.0007 \\ -0.0200 & 0.0003 & 0.9998 \end{pmatrix}$	$\mathbf{F}_{12}$(b)
	Q_{12}^{-}		$\hat{\mathbf{m}}_{\mathbf{12}}$(c) [0.7245 0.0253 0.6888]	$\mathbf{R}_{12}$ (c) $\begin{pmatrix} 0.9996 & -0.0187 & -0.0200 \\ 0.0187 & 0.9998 & -0.0007 \\ 0.0200 & 0.0003 & 0.9998 \end{pmatrix}$	$\mathbf{F}_{12}$(c)
			$\hat{\mathbf{m}}_{\mathbf{12}}$(d) [0.7245 0.0253 -0.6888]	$\mathbf{R}_{12}$ (d) $\begin{pmatrix} 0.9996 & -0.0187 & 0.0200 \\ 0.0187 & 0.9998 & 0.0007 \\ -0.0200 & -0.0003 & 0.9998 \end{pmatrix}$	$\mathbf{F}_{12}$(d)
M_2M_1	Q_{21}^{+}	0.6823	$\hat{\mathbf{m}}_{\mathbf{21}}$(a) [-0.0253 0.7245 0.6888]	$\mathbf{R}_{21}$(a) $\begin{pmatrix} 0.9998 & -0.0187 & 0.0007 \\ 0.0187 & 0.9996 & -0.0200 \\ -0.0003 & 0.0200 & 0.9998 \end{pmatrix}$	$\mathbf{F}_{21}$(a)
			$\hat{\mathbf{m}}_{\mathbf{21}}$(b) [-0.0253 0.7245 -0.6888]	$\mathbf{R}_{21}$ (b) $\begin{pmatrix} 0.9998 & -0.0187 & -0.0007 \\ 0.0187 & 0.9996 & 0.0200 \\ 0.0003 & -0.0200 & 0.9998 \end{pmatrix}$	$\mathbf{F}_{21}$(b)
	Q_{21}^{-}		$\hat{\mathbf{m}}_{\mathbf{21}}$(c) [0.0253 0.7245 0.6888]	$\mathbf{R}_{21}$ (c) $\begin{pmatrix} 0.9998 & 0.0187 & -0.0007 \\ -0.0187 & 0.9996 & -0.0200 \\ 0.0003 & 0.0200 & 0.9998 \end{pmatrix}$	$\mathbf{F}_{21}$(c)
			$\hat{\mathbf{m}}_{\mathbf{21}}$(d) [0.0253 0.7245 -0.6888]	$\mathbf{R}_{21}$ (d) $\begin{pmatrix} 0.9998 & 0.0187 & 0.0007 \\ -0.0187 & 0.9996 & 0.0200 \\ -0.0003 & -0.0200 & 0.9998 \end{pmatrix}$	$\mathbf{F}_{21}$(d)
M_1M_3	Q_{13}^{+}	0.6823	$\hat{\mathbf{m}}_{\mathbf{13}}$(a) [-0.7245 0.6888 0.0253]	$\mathbf{R}_{13}$ (a) $\begin{pmatrix} 0.9996 & 0.0200 & 0.0187 \\ -0.0200 & 0.9998 & 0.0003 \\ -0.0187 & -0.0007 & 0.9998 \end{pmatrix}$	$\mathbf{F}_{13}$(a)
			$\hat{\mathbf{m}}_{\mathbf{13}}$(b) [-0.7245 -0.6888 0.0253]	$\mathbf{R}_{13}$ (b) $\begin{pmatrix} 0.9996 & -0.0200 & 0.0187 \\ 0.0200 & 0.9998 & -0.0003 \\ -0.0187 & 0.0007 & 0.9998 \end{pmatrix}$	$\mathbf{F}_{13}$(b)
	Q_{13}^{-}		$\hat{\mathbf{m}}_{\mathbf{13}}$(c) [0.7245 -0.6888 0.0253]	$\mathbf{R}_{13}$ (c) $\begin{pmatrix} 0.9996 & 0.0200 & -0.0187 \\ -0.0200 & 0.9998 & -0.0003 \\ 0.0187 & 0.0007 & 0.9998 \end{pmatrix}$	$\mathbf{F}_{13}$(c)
			$\hat{\mathbf{m}}_{\mathbf{13}}$(d) [0.7245 0.6888 0.0253]	$\mathbf{R}_{13}$ (d) $\begin{pmatrix} 0.9996 & -0.0200 & -0.0187 \\ 0.0200 & 0.9998 & 0.0003 \\ 0.0187 & -0.0007 & 0.9998 \end{pmatrix}$	$\mathbf{F}_{13}$(d)

Table A2(continue)

Twin M_iM_j	$\mathbf{Q}_{ij}$ acting on Mj	λ_{ij}	Normal of the habit plane $\hat{\mathbf{m}}_{ij}$	Rotation acting on M_iM_j R_{ij}	Deformation gradient $\mathbf{F}_{ij}$
M_3M_1	Q_{31}^{+}	0.6823	$\hat{\mathbf{m}}_{\mathbf{31}}$(a) [-0.0253 -0.6888 0.7245]	$\mathbf{R}_{31}$(a) $\begin{pmatrix} 0.9998 & -0.0007 & -0.0187 \\ 0.0003 & 0.9998 & -0.0200 \\ 0.0187 & 0.0200 & 0.9996 \end{pmatrix}$	$\mathbf{F}_{31}$(a)
			$\hat{\mathbf{m}}_{\mathbf{31}}$(b) [-0.0253 0.6888 0.7245]	$\mathbf{R}_{31}$ (b) $\begin{pmatrix} 0.9998 & 0.0007 & -0.0187 \\ -0.0003 & 0.9998 & 0.0200 \\ 0.0187 & -0.0200 & 0.9996 \end{pmatrix}$	$\mathbf{F}_{31}$(b)
	$Q_{\bar{3}1}^{-}$		$\hat{\mathbf{m}}_{\mathbf{31}}$(c) [0.0253 0.6888 0.7245]	$\mathbf{R}_{31}$ (c) $\begin{pmatrix} 0.9998 & -0.0007 & 0.0187 \\ 0.0003 & 0.9998 & 0.0200 \\ -0.0187 & -0.0200 & 0.9996 \end{pmatrix}$	$\mathbf{F}_{31}$(c)
			$\hat{\mathbf{m}}_{\mathbf{31}}$(d) [0.0253 -0.6888 0.7245]	$\mathbf{R}_{31}$ (d) $\begin{pmatrix} 0.9998 & 0.0007 & 0.0187 \\ -0.0003 & 0.9998 & -0.0200 \\ -0.0187 & 0.0200 & 0.9996 \end{pmatrix}$	$\mathbf{F}_{31}$(d)
M_2M_3	Q_{23}^{+}	0.6823	$\hat{\mathbf{m}}_{\mathbf{23}}$(a) [0.6888 0.7245 -0.0253]	$\mathbf{R}_{23}$(a) $\begin{pmatrix} 0.9998 & 0.0200 & -0.0003 \\ -0.0200 & 0.9996 & 0.0187 \\ 0.0007 & -0.0187 & 0.9998 \end{pmatrix}$	$\mathbf{F}_{23}$(a)
			$\hat{\mathbf{m}}_{\mathbf{23}}$(b) [-0.6888 0.7245 -0.0253]	$\mathbf{R}_{23}$ (b) $\begin{pmatrix} 0.9998 & -0.0200 & 0.0003 \\ 0.0200 & 0.9996 & 0.0187 \\ -0.0007 & -0.0187 & 0.9998 \end{pmatrix}$	$\mathbf{F}_{23}$(b)
	$Q_{\bar{2}3}^{-}$		$\hat{\mathbf{m}}_{\mathbf{23}}$(c) [0.6888 0.7245 0.0253]	$\mathbf{R}_{23}$ (c) $\begin{pmatrix} 0.9998 & 0.0200 & 0.0003 \\ -0.0200 & 0.9996 & -0.0187 \\ -0.0007 & 0.0187 & 0.9998 \end{pmatrix}$	$\mathbf{F}_{23}$(c)
			$\hat{\mathbf{m}}_{\mathbf{23}}$(d) [-0.6888 0.7245 0.0253]	$\mathbf{R}_{23}$ (d) $\begin{pmatrix} 0.9998 & -0.0200 & -0.0003 \\ 0.0200 & 0.9996 & -0.0187 \\ 0.0007 & 0.0187 & 0.9998 \end{pmatrix}$	$\mathbf{F}_{23}$(d)
M_3M_2	Q_{32}^{+}	0.6823	$\hat{\mathbf{m}}_{\mathbf{32}}$(a) [0.6888 -0.0253 0.7245]	$\mathbf{R}_{32}$ (a) $\begin{pmatrix} 0.9998 & -0.0003 & 0.0200 \\ 0.0007 & 0.9998 & -0.0187 \\ -0.0200 & 0.0187 & 0.9996 \end{pmatrix}$	$\mathbf{F}_{32}$(a)
			$\hat{\mathbf{m}}_{\mathbf{32}}$(b) [-0.6888 -0.0253 0.7245]	$\mathbf{R}_{32}$ (b) $\begin{pmatrix} 0.9998 & 0.0003 & -0.0200 \\ -0.0007 & 0.9998 & -0.0187 \\ 0.0200 & 0.0187 & 0.9996 \end{pmatrix}$	$\mathbf{F}_{32}$(b)
	$Q_{\bar{3}2}^{-}$		$\hat{\mathbf{m}}_{\mathbf{32}}$(c) [0.6888 0.0253 0.7245]	$\mathbf{R}_{32}$ (c) $\begin{pmatrix} 0.9998 & 0.0003 & 0.0200 \\ -0.0007 & 0.9998 & 0.0187 \\ -0.0200 & -0.0187 & 0.9996 \end{pmatrix}$	$\mathbf{F}_{32}$(c)
			$\hat{\mathbf{m}}_{\mathbf{32}}$(d) [-0.6888 0.0253 0.7245]	$\mathbf{R}_{32}$ (d) $\begin{pmatrix} 0.9998 & -0.0003 & -0.0200 \\ 0.0007 & 0.9998 & 0.0187 \\ 0.0200 & -0.0187 & 0.9996 \end{pmatrix}$	$\mathbf{F}_{32}$(d)

3. *Global compatibility of the experimentally observed five-domain structure*

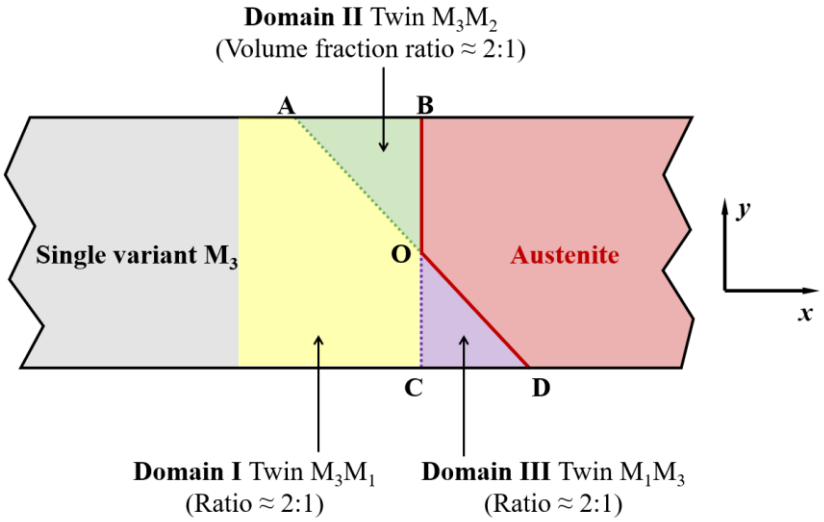

Fig. A1 The schematic of the experimentally observed five-domain structure.

Based on the experimental observation (as shown in Fig. A1), the compatibility equations for habit planes OB and OD can be formulated as follows.

For habit plane OB with the twin M_3M_2:

$$\begin{cases} \mathbf{Q}_{32}\mathbf{U}_2 - \mathbf{U}_3 = \mathbf{a}_{32} \otimes \hat{\mathbf{n}}_{32} & \text{(A.7)} \\ \mathbf{U}_{32} = \lambda_{32}\mathbf{U}_3 + (1-\lambda_{32})\,\mathbf{Q}_{32}\mathbf{U}_2, & \text{(A.8)} \\ \mathbf{F}_{32} - \mathbf{I} = \mathbf{b}_{32} \otimes \hat{\mathbf{m}}_{32} & \text{(A.9)} \end{cases}$$

where $\mathbf{F}_{32} = \mathbf{R}_{32}\mathbf{U}_{32}$ and λ_{32} is the volume fraction of the variants $\mathbf{U}_3$ in the twin $\mathbf{U}_{32}$.

For habit plane OD:

$$\begin{cases} \mathbf{Q}_{13}\mathbf{U}_3 - \mathbf{U}_1 = \mathbf{a}_{13} \otimes \hat{\mathbf{n}}_{13} & \text{(A.10)} \\ \mathbf{U}_{13} = \lambda_{13}\mathbf{U}_1 + (1-\lambda_{13})\,\mathbf{Q}_{13}\mathbf{U}_3, & \text{(A.11)} \\ \mathbf{F}_{13} - \mathbf{I} = \mathbf{b}_{13} \otimes \hat{\mathbf{m}}_{13} & \text{(A.12)} \end{cases}$$

where $\mathbf{F}_{13} = \mathbf{R}_{13}\mathbf{U}_{13}$ and $\lambda_{13}$is the volume fraction of the variants $\mathbf{U}_1$ in the twin $\mathbf{U}_{13}$.

By solving Eqs. (A.7) ~ (A.12) (results in Table A2) and comparison with Fig. A1, we obtain four solutions of $\mathbf{F}_{32}$ (e.g., $\mathbf{F}_{32}$ (a) ~ (d)) and two solutions of $\mathbf{F}_{13}$ (e.g., $\mathbf{F}_{13}$ (b) and (d)) that can describe the two domains (twins M_3M_2 and M_1M_3) with the observed habit planes OB and OD, whose traces (or projections) on the *x*-*y* plane are approximately vertical and 45° to *x*-axis, respectively.

The compatibility between twins M_3M_1 and M_3M_2 separated by the domain wall OA can be described by equations below:

$$\begin{cases} \mathbf{Q}_{31}\mathbf{U}_1 - \mathbf{U}_3 = \mathbf{a}_{31} \otimes \hat{\mathbf{n}}_{31} & \text{(A.13)} \\ \mathbf{U}_{31} = \lambda_{31}\mathbf{U}_3 + (1-\lambda_{31})\,\mathbf{Q}_{31}\mathbf{U}_1, & \text{(A.14)} \\ \mathbf{F}_{31} - \mathbf{F}_{32} = \mathbf{b}_{3231} \otimes \hat{\mathbf{m}}_{3231} & \text{(A.15)} \end{cases}$$

where $\mathbf{F}_{31} = \mathbf{R}_{3231}\mathbf{U}_{31}$ and λ_{31} is the volume fraction of the variants $\mathbf{U}_3$ in the twin $\mathbf{U}_{31}$. Similar to the solution procedures above, we calculate the matrix $\mathrm{C} = \mathbf{F}_{32}{}^{-\mathrm{T}}\,\mathbf{U}_{31}{}^{\mathrm{T}}\,\mathbf{U}_{31}\,\mathbf{F}_{32}{}^{-1}$, whose eigenvalues α_1, α_2, and α_3 now depend on the volume fraction λ_{31}. To satisfy the compatible condition in Eq. (A.15), one of the eigenvalues must be one, and the other two should be greater than one and smaller than one, respectively. As a result, we obtain two λ_{31} values ($\lambda_{31} \approx 1$ or $\lambda_{31} \approx 0.6823$), and $\lambda_{31} \approx 0.6823$ is utilized because this value is consistent with our experimental observation. Based on the obtained λ_{31}, the solutions to Eq. (A.15) are shown in Table A3, among which only 8 solutions (marked in grey, $\hat{\mathbf{m}}_{3231} \approx$ [1 1 0] or [-1 -1 0]) can capture the experimentally observed domain wall OA (whose trace (or projection) on the *x*-*y* plane is around 45° to the *x*-axis).

Table A3 Compatibility between twin M_3M_2 (whose deformation gradient $\mathbf{F}_{32}$ has been already verified to be compatible with austenite in Table A2) and twin M_3M_1 (whose deformation gradient $\mathbf{F}_{31}$ is currently solved) for the five-domain structure. The solutions marked in grey are consistent with the experimental observation.

Deformation matrix $\mathbf{F}_{32}$	$\mathbf{Q}_{31}$ acting on M_1	λ_{31}	Normal of the twin-twin plane $\hat{\mathbf{m}}_{3231}$	Rotation acting on M_3M_1 $\mathbf{R}_{3231}$	Deformation gradient $\mathbf{F}_{31}$
$\mathbf{F}_{32}$(a)	Q_{31}^{+}	0.6823	$\hat{\mathbf{m}}_{\mathbf{3231}}$(a) [0.7061 0.7061 -0.5544]	$\mathbf{R}_{3231}$(a) $\begin{pmatrix} 0.9998 & -0.0194 & 0.0021 \\ 0.0194 & 0.9998 & -0.0011 \\ -0.0021 & 0.0011 & 1 \end{pmatrix}$	$\mathbf{F}_{31}$(a)
			$\hat{\mathbf{m}}_{\mathbf{3231}}$(b) [0.7071 -0.7071 0]	$\mathbf{R}_{3231}$ (b) $\begin{pmatrix} 0.9998 & 0.0180 & 0.0006 \\ -0.0180 & 0.9998 & 0.0011 \\ -0.0006 & -0.0011 & 1 \end{pmatrix}$	$\mathbf{F}_{31}$**(b)**
	Q_{31}^{-}		$\hat{\mathbf{m}}_{\mathbf{3231}}$(c) [0.7061 -0.7061 0.0544]	$\mathbf{R}_{3231}$(c) $\begin{pmatrix} 0.9991 & 0.0180 & 0.0380 \\ -0.0180 & 0.9998 & -0.0011 \\ -0.0380 & 0.0004 & 0.9993 \end{pmatrix}$	$\mathbf{F}_{31}$(c)
			$\hat{\mathbf{m}}_{\mathbf{3231}}$(d) [0.7071 0.7071 0]	$\mathbf{R}_{3231}$(d) $\begin{pmatrix} 0.9990 & -0.0194 & 0.0394 \\ 0.0194 & 0.9998 & 0.0011 \\ -0.0395 & -0.0004 & 0.9992 \end{pmatrix}$	$\mathbf{F}_{31}$(d)
$\mathbf{F}_{32}$(b)	Q_{31}^{+}	0.6823	$\hat{\mathbf{m}}_{\mathbf{3231}}$(e) [0.7071 -0.7071 0]	$\mathbf{R}_{3231}$(e) $\begin{pmatrix} 0.9990 & 0.0194 & -0.0394 \\ -0.0194 & 0.9998 & 0.0011 \\ 0.0395 & -0.0004 & 0.9992 \end{pmatrix}$	$\mathbf{F}_{31}$(e)
			$\hat{\mathbf{m}}_{\mathbf{3231}}$(f) [0.7061 0.7061 -0.5544]	$\mathbf{R}_{3231}$(f) $\begin{pmatrix} 0.9991 & -0.0180 & -0.0380 \\ 0.0180 & 0.9998 & -0.0011 \\ 0.0380 & 0.0004 & 0.9993 \end{pmatrix}$	$\mathbf{F}_{31}$(f)
	Q_{31}^{-}		$\hat{\mathbf{m}}_{\mathbf{3231}}$(g) [0.7071 0.7071 0]	$\mathbf{R}_{3231}$(g) $\begin{pmatrix} 0.9998 & -0.0180 & -0.0006 \\ 0.0180 & 0.9998 & 0.0011 \\ 0.0006 & -0.0011 & 1 \end{pmatrix}$	$\mathbf{F}_{31}$(g)
			$\hat{\mathbf{m}}_{\mathbf{3231}}$(h) [0.7061 -0.7061 0.0544]	$\mathbf{R}_{3231}$(h) $\begin{pmatrix} 0.9998 & 0.0194 & -0.0021 \\ -0.0194 & 0.9998 & -0.0011 \\ 0.0021 & 0.0011 & 1 \end{pmatrix}$	$\mathbf{F}_{31}$(h)

Table A3(continue)

Deformation matrix $\mathbf{F}_{32}$	$\mathbf{Q}_{31}$ acting on M_1	λ_{31}	Normal of the twin-twin plane $\hat{\mathbf{m}}_{3231}$	Rotation acting on M_3M_1 $\mathbf{R}_{3231}$	Deformation gradient $\mathbf{F}_{31}$
$\mathbf{F}_{32}$(c)	Q_{31}^{+}	0.6823	$\hat{\mathbf{m}}_{\mathbf{3231}}$(i) [0.7061 -0.7061 -0.5544]	$\mathbf{R}_{3231}$(i) $\begin{pmatrix} 0.9998 & 0.0194 & 0.0021 \\ -0.0194 & 0.9998 & 0.0011 \\ -0.0021 & -0.0011 & 1 \end{pmatrix}$	$\mathbf{F}_{31}$(i)
			$\hat{\mathbf{m}}_{\mathbf{3231}}$(j) [0.7071 0.7071 0]	$\mathbf{R}_{3231}$(j) $\begin{pmatrix} 0.9998 & -0.0180 & 0.0006 \\ 0.0180 & 0.9998 & -0.0011 \\ -0.0006 & 0.0011 & 1 \end{pmatrix}$	$\mathbf{F}_{31}$(j)
	Q_{31}^{-}		$\hat{\mathbf{m}}_{\mathbf{3231}}$(k) [0.7061 0.7061 0.0544]	$\mathbf{R}_{3231}$(k) $\begin{pmatrix} 0.9991 & -0.0180 & 0.0380 \\ 0.0180 & 0.9998 & 0.0011 \\ -0.0380 & -0.0004 & 0.9993 \end{pmatrix}$	$\mathbf{F}_{31}$(k)
			$\hat{\mathbf{m}}_{\mathbf{3231}}$(l) [0.7071 -0.7071 0]	$\mathbf{R}_{3231}$(l) $\begin{pmatrix} 0.9990 & 0.0194 & 0.0394 \\ -0.0194 & 0.9998 & -0.0011 \\ -0.0395 & 0.0004 & 0.9992 \end{pmatrix}$	$\mathbf{F}_{31}$(l)
$\mathbf{F}_{32}$(d)	Q_{31}^{+}	0.6823	$\hat{\mathbf{m}}_{\mathbf{3231}}$(m) [0.7071 0.7071 0]	$\mathbf{R}_{3231}$(m) $\begin{pmatrix} 0.9990 & -0.0194 & -0.0394 \\ 0.0194 & 0.9998 & -0.0011 \\ 0.0395 & 0.0004 & 0.9992 \end{pmatrix}$	$\mathbf{F}_{31}$(m)
			$\hat{\mathbf{m}}_{\mathbf{3231}}$(n) [0.7061 -0.7061 -0.0544]	$\mathbf{R}_{3231}$(n) $\begin{pmatrix} 0.9991 & 0.0180 & -0.0380 \\ -0.0180 & 0.9998 & 0.0011 \\ 0.0380 & -0.0004 & 0.9993 \end{pmatrix}$	$\mathbf{F}_{31}$(n)
	Q_{31}^{-}		$\hat{\mathbf{m}}_{\mathbf{3231}}$(o) [0.7071 -0.7071 0]	$\mathbf{R}_{3231}$(o) $\begin{pmatrix} 0.9998 & 0.0180 & -0.0006 \\ -0.0180 & 0.9998 & -0.0011 \\ 0.0006 & 0.0011 & 1 \end{pmatrix}$	$\mathbf{F}_{31}$(o)
			$\hat{\mathbf{m}}_{\mathbf{3231}}$(p) [0.7061 0.7061 0.0544]	$\mathbf{R}_{3231}$(p) $\begin{pmatrix} 0.9998 & -0.0194 & -0.0021 \\ 0.0194 & 0.9998 & 0.0011 \\ 0.0021 & -0.0011 & 1 \end{pmatrix}$	$\mathbf{F}_{31}$(p)

Now, we obtain all the deformation matrices of $\mathbf{F}_{13}$ (2 solutions) and $\mathbf{F}_{31}$ (8 solutions) that are consistent with the experimental observation, but none of them satisfy Eq. (A.16):

$$\mathbf{F}_{31} - \mathbf{F}_{13} = \mathbf{b}_{1331} \otimes \hat{\mathbf{m}}_{1331} \tag{A.16}$$

According to (Balandraud et al., 2010), an extra rotation matrix $\mathbf{R}$ can be added in Eq. (A.16) to achieve the "compatibility":

$$\mathbf{R}\,\mathbf{F}_{31} - \mathbf{F}_{13} = \mathbf{b}_{1331} \otimes \hat{\mathbf{m}}_{1331} \tag{A.17}$$

With the solution to Eq. (A.17), there are three indicators in the literature to estimate the non-compatibility: the rotation angle ψ, the mismatch angle φ, and the non-coplanarity angle θ as defined in Eqs. (20) ~ (22).

The solutions to Eq. (A.17), which are consistent with the experimental observation, and their corresponding non-compatibility indicators are listed in Table A4.

Table A4 The calculation details of the compatibility between $\mathbf{F}_{13}$ and $\mathbf{F}_{31}$ (which are consistent with the experimental observation), for the five-domain structure, and their corresponding non-compatibility indicators.

Deformation matrix		Normal of the twin-twin plane $\hat{\mathbf{m}}_{1331}$	Corresponding $\mathbf{F}_{32}$	Rotation angle ψ (°)	Mismatch angle φ (°)	Non-coplanarity angle θ (°)	Order after sorting by angle ψ
$\mathbf{F}_{13}$	$\mathbf{F}_{31}$						
$\mathbf{F}_{13}$(b)	$\mathbf{F}_{31}$(a)	[-0.7071 0 -0.7071]	$\mathbf{F}_{32}$(a) with $\hat{\mathbf{m}}_{32}$(a) [0.6888 -0.0253 0.7245]	0.0612	0.0606	0.5111	**3**
		[0.7071 0 -0.7071]		2.4186	2.4182	70.2299	**25**
	$\mathbf{F}_{31}$(d)	[0.6820 0 -0.7313]		2.4258	2.4257	67.221	**31**
		[-0.7313 0 -0.6820]		0.0824	0.0437	3.92	**5**
$\mathbf{F}_{13}$(d)	$\mathbf{F}_{31}$(a)	[0.6820 0 0.7313]		0.1196	0.1110	2.5595	**7**
		[-0.7313 0 0.6820]		2.4239	2.4218	73.0426	**29**
	$\mathbf{F}_{31}$(d)	[-0.7071 0 -0.7071]		0.0555	0.0542	0.6922	**1**
		[0.7071 0 -0.7071]		2.4222	2.4219	69.9423	**27**
$\mathbf{F}_{13}$(b)	$\mathbf{F}_{31}$(f)	[-0.7071 0 -0.7071]	$\mathbf{F}_{32}$(b) with $\hat{\mathbf{m}}_{32}$(b) [-0.6888 -0.0253 0.7245]	2.3389	2.3369	66.916	**19**
		[0.7071 0 -0.7071]		0.1708	0.1567	4.3191	**9**
	$\mathbf{F}_{31}$(g)	[0.6820 0 -0.7313]		0.2045	0.2040	0.8533	**15**
		[-0.7313 0 -0.6820]		2.3407	2.3354	69.8405	**21**
$\mathbf{F}_{13}$(d)	$\mathbf{F}_{31}$(f)	[0.6820 0 0.7313]		2.3424	2.3420	64.2001	**23**
		[-0.7313 0 0.6820]		0.1828	0.1345	7.6672	**13**
	$\mathbf{F}_{31}$(g)	[-0.7071 0 -0.7071]		2.3353	2.3331	67.0371	**17**
		[0.7071 0 -0.7071]		0.1754	0.1629	4.0332	**11**
$\mathbf{F}_{13}$(b)	$\mathbf{F}_{31}$(j)	[-0.7071 0 -0.7071]	$\mathbf{F}_{32}$(c) with $\hat{\mathbf{m}}_{32}$(c) [0.6888 0.0253 0.7245]	0.1754	0.1629	4.0332	**12**
		[0.7071 0 -0.7071]		2.3353	2.3331	67.0371	**18**
	$\mathbf{F}_{31}$(k)	[0.6820 0 -0.7313]		2.3424	2.3420	64.2001	**24**
		[-0.7313 0 -0.6820]		0.1828	0.1345	7.6672	**14**
$\mathbf{F}_{13}$(d)	$\mathbf{F}_{31}$(j)	[0.6820 0 0.7313]		0.2045	0.2040	0.8533	**16**
		[-0.7313 0 0.6820]		2.3407	2.3354	69.8405	**22**
	$\mathbf{F}_{31}$(k)	[-0.7071 0 -0.7071]		0.1708	0.1567	4.3191	**10**
		[0.7071 0 -0.7071]		2.3389	2.3369	66.9160	**20**
$\mathbf{F}_{13}$(b)	$\mathbf{F}_{31}$(m)	[-0.7071 0 -0.7071]	$\mathbf{F}_{32}$(d) with $\hat{\mathbf{m}}_{32}$(d) [-0.6888 0.0253 0.7245]	2.4222	2.4219	69.9423	**28**
		[0.7071 0 -0.7071]		0.0555	0.0542	0.6922	**2**
	$\mathbf{F}_{31}$(p)	[0.6820 0 -0.7313]		0.1196	0.1110	2.5595	**8**
		[-0.7313 0 -0.6820]		2.4239	2.4218	73.0426	**30**
$\mathbf{F}_{13}$(d)	$\mathbf{F}_{31}$(m)	[0.6820 0 0.7313]		2.4258	2.4257	67.221	**32**
		[-0.7313 0 0.6820]		0.0824	0.0437	3.92	**6**
	$\mathbf{F}_{31}$(p)	[-0.7071 0 -0.7071]		2.4186	2.4182	70.2299	**26**
		[0.7071 0 -0.7071]		0.0612	0.0606	0.5111	**4**

Appendix B: *Compatibility of the experimentally observed four-domain structure*

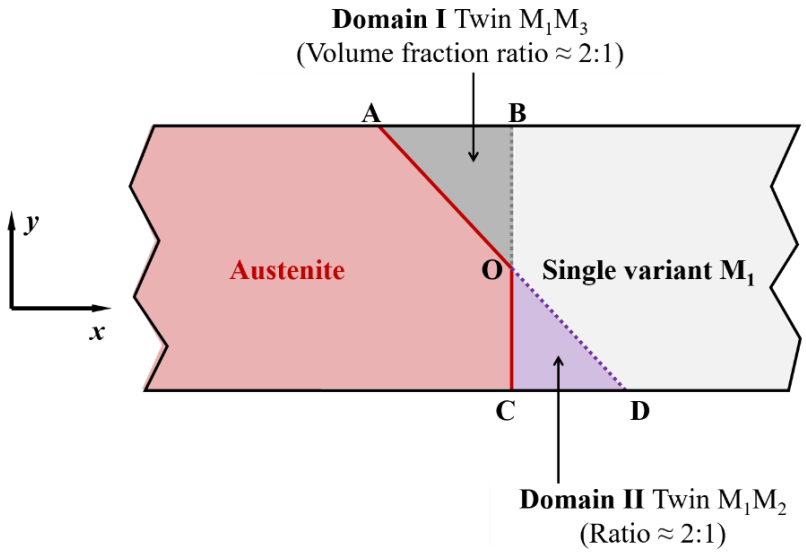

Fig. B1 The schematic of the experimentally observed four-domain structure.

In our previous experiments on the same material (Ni-Mn-Ga single crystal) (Qin et al., 2023), a four-domain interfacial structure consisting of the M_1 variant, twin M_1M_3, twin M_1M_2 and austenite was observed, as schematically shown in Fig. B1. The compatibility of the domain walls can be formulated as follows:

For habit plane OA:

$$\begin{cases} \mathbf{Q}_{12}\mathbf{U}_2 - \mathbf{U}_1 = \mathbf{a}_{12} \otimes \hat{\mathbf{n}}_{12} & \text{(B.1)} \\ \mathbf{U}_{12} = \lambda_{12}\mathbf{U}_1 + (1-\lambda_{12})\,\mathbf{Q}_{12}\mathbf{U}_2, & \text{(B.2)} \\ \mathbf{F}_{12} - \mathbf{I} = \mathbf{b}_{12} \otimes \hat{\mathbf{m}}_{12} & \text{(B.3)} \end{cases}$$

where $\mathbf{F}_{12} = \mathbf{R}_{12}\mathbf{U}_{12}$ and λ_{12} is the volume fraction of the variant $\mathbf{U}_1$ in the twin $\mathbf{U}_{12}$.

For habit plane OC:

$$\begin{cases} \mathbf{Q}_{13}\mathbf{U}_3 - \mathbf{U}_1 = \mathbf{a}_{13} \otimes \hat{\mathbf{n}}_{13} & \text{(B.4)} \\ \mathbf{U}_{13} = \lambda_{13}\mathbf{U}_1 + (1-\lambda_{13})\,\mathbf{Q}_{13}\mathbf{U}_3, & \text{(B.5)} \\ \mathbf{F}_{13} - \mathbf{I} = \mathbf{b}_{13} \otimes \hat{\mathbf{m}}_{13} & \text{(B.6)} \end{cases}$$

where $\mathbf{F}_{13} = \mathbf{R}_{13}\mathbf{U}_{13}$ and λ_{13} is the volume fraction of the variant $\mathbf{U}_1$ in the twin $\mathbf{U}_{13}$. The solutions to the above habit planes are already shown in Table A2 of Appendix A.

For domain wall OD:

$$\mathbf{F}_1 - \mathbf{F}_{12} = \mathbf{b}_{121} \otimes \hat{\mathbf{m}}_{121} \tag{B.7}$$

where $\mathbf{F}_1 = \mathbf{R}_{121}\mathbf{U}_1$. With the given $\mathbf{F}_{12}$ of Table A2, the solutions of $\mathbf{F}_1$ to Eq. (B.7) are listed in Table B1.

Table B1 Compatibility planes between the single variant M_1 and the twin M_1M_2 (whose deformation gradient $\mathbf{F}_{12}$ is already verified to be compatible with austenite in Table A2) for the four-domain structure.

Deformation matrix $\mathbf{F}_{32}$	Normal of the twin-twin plane $\hat{\mathbf{m}}_{121}$	Rotation acting on M_3M_1 $\mathbf{R}_{121}$	Deformation gradient $\mathbf{F}_1$
$\mathbf{F}_{12}$(a)	$\hat{\mathbf{m}}_{121}$(a) [0.6782 0.7349 0]	$\mathbf{R}_{121}$(a) $\begin{pmatrix} 0.9996 & -0.0187 & -0.0200 \\ 0.0187 & 0.9998 & 0.0007 \\ 0.0200 & -0.0011 & 0.9998 \end{pmatrix}$	$\mathbf{F}_1$(a)
	$\hat{\mathbf{m}}_{121}$(b) [0.7071 -0.7071 0]	$\mathbf{R}_{121}$(b) $\begin{pmatrix} 0.9996 & 0.0187 & -0.0200 \\ -0.0187 & 0.9998 & 0.0007 \\ 0.0200 & -0.0003 & 0.9998 \end{pmatrix}$	$\mathbf{F}_1$(b)
$\mathbf{F}_{12}$(b)	$\hat{\mathbf{m}}_{121}$(c) [0.6782 0.7349 0]	$\mathbf{R}_{121}$(c) $\begin{pmatrix} 0.9996 & -0.0187 & 0.0200 \\ 0.0187 & 0.9998 & -0.0007 \\ -0.0200 & 0.0011 & 0.9998 \end{pmatrix}$	$\mathbf{F}_1$(c)
	$\hat{\mathbf{m}}_{121}$(d) [0.7071 -0.7071 0]	$\mathbf{R}_{121}$(d) $\begin{pmatrix} 0.9996 & 0.0187 & 0.0200 \\ -0.0187 & 0.9998 & -0.0007 \\ 0.0200 & -0.0003 & 0.9998 \end{pmatrix}$	$\mathbf{F}_1$(d)
$\mathbf{F}_{12}$(c)	$\hat{\mathbf{m}}_{121}$(e) [0.7071 0.7071 0]	$\mathbf{R}_{121}$(e) $\begin{pmatrix} 0.9996 & -0.0187 & -0.0200 \\ 0.0187 & 0.9998 & -0.0007 \\ 0.0200 & 0.0003 & 0.9998 \end{pmatrix}$	$\mathbf{F}_1$(e)
	$\hat{\mathbf{m}}_{121}$(f) [0.6782 -0.7349 0]	$\mathbf{R}_{121}$(f) $\begin{pmatrix} 0.9996 & 0.0187 & -0.0200 \\ -0.0187 & 0.9998 & -0.0007 \\ 0.0200 & 0.0011 & 0.9998 \end{pmatrix}$	$\mathbf{F}_1$(f)
$\mathbf{F}_{12}$(d)	$\hat{\mathbf{m}}_{121}$(g) [0.7071 0.7071 0]	$\mathbf{R}_{121}$(g) $\begin{pmatrix} 0.9996 & -0.0187 & 0.0200 \\ 0.0187 & 0.9998 & 0.0007 \\ -0.0200 & -0.0003 & 0.9998 \end{pmatrix}$	$\mathbf{F}_1$(g)
	$\hat{\mathbf{m}}_{121}$(h) [0.6782 -0.7349 0]	$\mathbf{R}_{121}$(h) $\begin{pmatrix} 0.9996 & 0.0187 & 0.0200 \\ -0.0187 & 0.9998 & 0.0007 \\ -0.0200 & -0.0011 & 0.9998 \end{pmatrix}$	$\mathbf{F}_1$(h)

Finally, we need to check the compatibility of the domain wall OB. It is easy to find that the Hadamard condition with the deformation matrices $\mathbf{F}_1$ and $\mathbf{F}_{13}$ derived above is not satisfied; i.e., there is no solution to the equation $\mathbf{F}_1 - \mathbf{F}_{13} = \mathbf{b}_{131} \otimes \hat{\mathbf{m}}_{131}$. An extra rotation $\mathbf{R}$ is needed to achieve the "compatibility":

$$\mathbf{R}\,\mathbf{F}_1 - \mathbf{F}_{13} = \mathbf{b}_{131} \otimes \hat{\mathbf{m}}_{131} \tag{B.8}$$

Solving Eqs. (B.1) ~ (B.8), we obtain four domain wall unit normals $\hat{\mathbf{m}}_{12}$, $\hat{\mathbf{m}}_{13}$, $\hat{\mathbf{m}}_{121}$, and $\hat{\mathbf{m}}_{131}$. The corresponding non-compatibility indicators ψ, φ, and θ defined in Eqs. (20) ~ (22) of the main text of the paper are:

$$\psi = \arccos\left(\frac{\mathrm{tr}\,\mathbf{R} - 1}{2}\right) \tag{B.9}$$

where **R** is the extra rotation from Eq. (B-8).

$$\varphi = \arccos\left(\frac{|\mathrm{n}_1 \cdot \mathrm{n}_2|}{|\mathrm{n}_1||\mathrm{n}_2|}\right) \tag{B.10}$$

where $\mathrm{n}_1 = (\mathbf{F}_{13})^{-\mathrm{T}}\hat{\mathbf{m}}_{131}$ and $\mathrm{n}_2 = (\mathbf{F}_1)^{-\mathrm{T}}\hat{\mathbf{m}}_{131}$ are normal of twin-twin planes in deformed configurations (domains of the twin M_1M_3 and the single variant M_1).

$$\theta = |\arcsin(\hat{\mathbf{v}} \wedge \hat{\mathbf{w}})| \tag{B.11}$$

where $\hat{\mathbf{v}} = \hat{\mathbf{m}}_{12} \wedge \hat{\mathbf{m}}_{13}$ and $\hat{\mathbf{w}} = \hat{\mathbf{m}}_{121} \wedge \hat{\mathbf{m}}_{131}$ denote the intersecting line of the two habit planes and the intersecting line of the two variant-twin planes, respectively.

The results (cases with slightly non-compatibility) of the domain wall normals and the indicators for the four-domain structure (consisting of the M_1 variant, twin M_1M_3, twin M_1M_2, and austenite) are listed in Table B2 and are plotted in Fig. B2, where all the values of ψ and φ are small, compared to 0.32° of the wedge pattern (Balandraud and Zanzotto, 2007). By contrast, there are only four cases with the angle θ much smaller than 2.5° of the X-interface of (Seiner et al., 2009). The four cases are marked in grey in Table B2 and highlighted in the orange circle in Fig. B2, and their schematics are shown in Fig. B3. The four cases with small non-compatibility indicators should be energetically preferred during the phase transformation. Interestingly, as shown by the schematics in Fig. B3, they are all X-interface rather than λ-interface. To verify the calculated 3D interface structures, more systematic experiments are needed in the future.

Table B2 All the possible solutions of the four-domain structure (consisting of the M_1 variant, twin M_1M_2, twin M_1M_3, and austenite) that satisfy the 'almost coplanarity' condition and their corresponding non-compatibility indicators.

Deformation matrix			Normal of the twin-twin plane $\hat{\mathbf{m}}_{121}$	Normal of the twin-twin plane $\hat{\mathbf{m}}_{131}$	Rotation angle ψ (°)	Mismatch angle φ (°)	Non-coplanarity angle θ (°)	Order after sorting by the angle θ
$\mathbf{F}_{12}$	$\mathbf{F}_{13}$	$\mathbf{F}_1$						
$\mathbf{F}_{12}$(a)	$\mathbf{F}_{13}$(a)	$\mathbf{F}_1$(b)	[0.7071 -0.7071 0]	[0.6782 0 0.7349]	0.1095	0.0836	2.3887	**5**
	$\mathbf{F}_{13}$(b)	$\mathbf{F}_1$(a)	[0.6782 0.7349 0]	[0.6782 0 0.7349]	0.1461	0.0766	4.5339	**15**
	$\mathbf{F}_{13}$(c)	$\mathbf{F}_1$(b)	[0.7071 -0.7071 0]	[0.7071 0 0.7071]	0.1244	0.1238	0.3919	**1**
	$\mathbf{F}_{13}$(d)	$\mathbf{F}_1$(a)	[0.6782 0.7349 0]	[0.7071 0 0.7071]	0.1095	0.0858	2.3887	**6**
$\mathbf{F}_{12}$(b)	$\mathbf{F}_{13}$(a)	$\mathbf{F}_1$(d)	[0.7071 -0.7071 0]	[0.7071 0 -0.7071]	0.1244	0.1238	0.3919	**2**
	$\mathbf{F}_{13}$(b)	$\mathbf{F}_1$(c)	[0.6782 0.7349 0]	[0.7071 0 -0.7071]	0.1095	0.0858	2.3887	**7**
	$\mathbf{F}_{13}$(c)	$\mathbf{F}_1$(d)	[0.7071 -0.7071 0]	[0.6782 0 -0.7349]	0.1095	0.0836	2.3887	**8**
	$\mathbf{F}_{13}$(d)	$\mathbf{F}_1$(c)	[0.6782 0.7349 0]	[0.6782 0 -0.7349]	0.1461	0.0766	4.5339	**13**
$\mathbf{F}_{12}$(c)	$\mathbf{F}_{13}$(a)	$\mathbf{F}_1$(f)	[0.6782 -0.7349 0]	[0.6782 0 0.7349]	0.1461	0.0766	4.5339	**16**
	$\mathbf{F}_{13}$(b)	$\mathbf{F}_1$(e)	[0.7071 0.7071 0]	[0.6782 0 0.7349]	0.1095	0.0836	2.3887	**9**
	$\mathbf{F}_{13}$(c)	$\mathbf{F}_1$(f)	[0.6782 -0.7349 0]	[0.7071 0 0.7071]	0.1095	0.0858	2.3887	**10**
	$\mathbf{F}_{13}$(d)	$\mathbf{F}_1$(e)	[0.7071 0.7071 0]	[0.7071 0 0.7071]	0.1244	0.1238	0.3919	**3**
$\mathbf{F}_{12}$(d)	$\mathbf{F}_{13}$(a)	$\mathbf{F}_1$(h)	[0.6782 -0.7349 0]	[0.7071 0 -0.7071]	0.1095	0.0858	2.3887	**11**
	$\mathbf{F}_{13}$(b)	$\mathbf{F}_1$(g)	[0.7071 0.7071 0]	[0.7071 0 -0.7071]	0.1244	0.1238	0.3919	**4**
	$\mathbf{F}_{13}$(c)	$\mathbf{F}_1$(h)	[0.6782 -0.7349 0]	[0.6782 0 -0.7349]	0.1461	0.0766	4.5339	**14**
	$\mathbf{F}_{13}$(d)	$\mathbf{F}_1$(g)	[0.7071 0.7071 0]	[0.6782 0 -0.7349]	0.1095	0.0836	2.3887	**12**

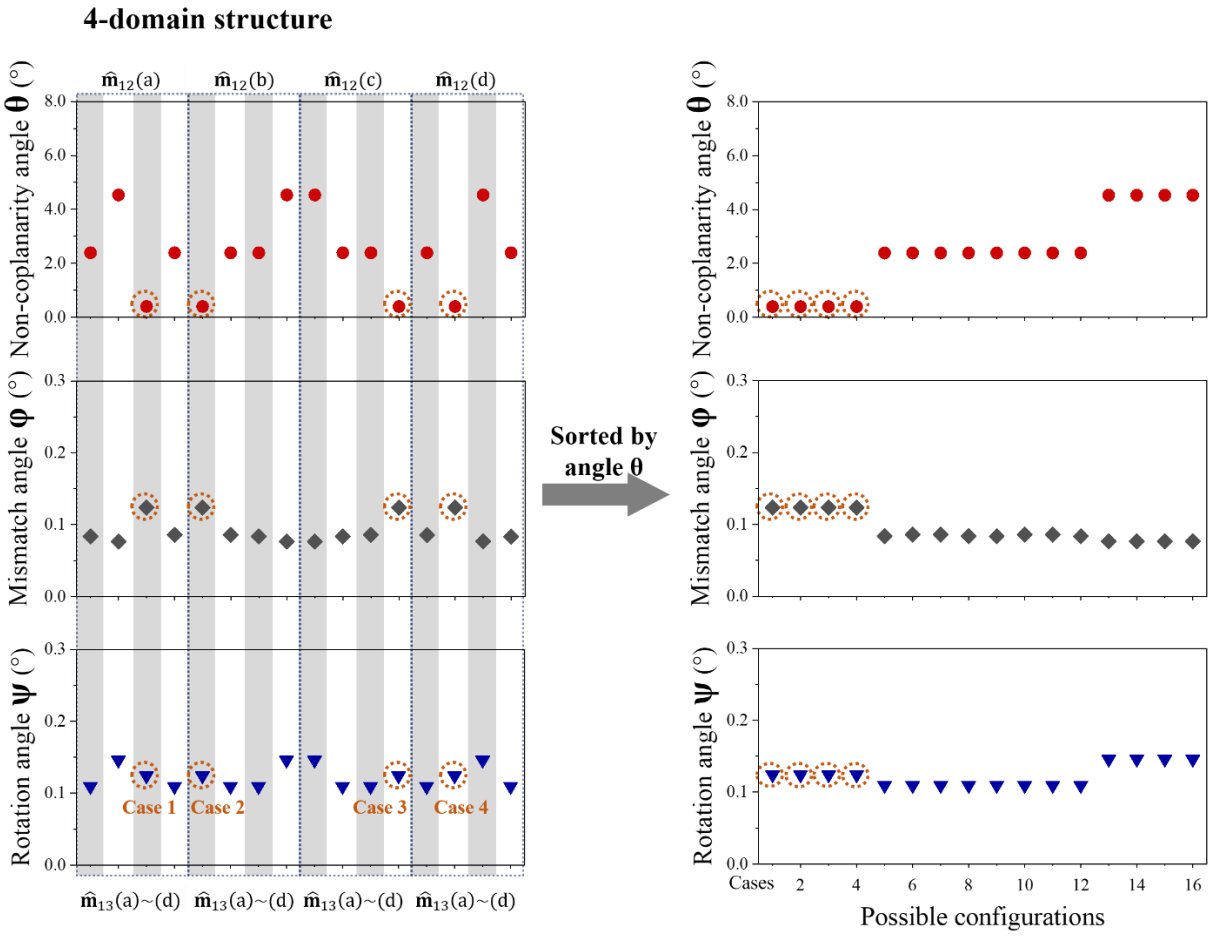

Fig. B2 The non-compatibility indicators of the four-domain structures (consisting of the M_1 variant, twin M_1M_2, twin M_1M_3, and austenite).

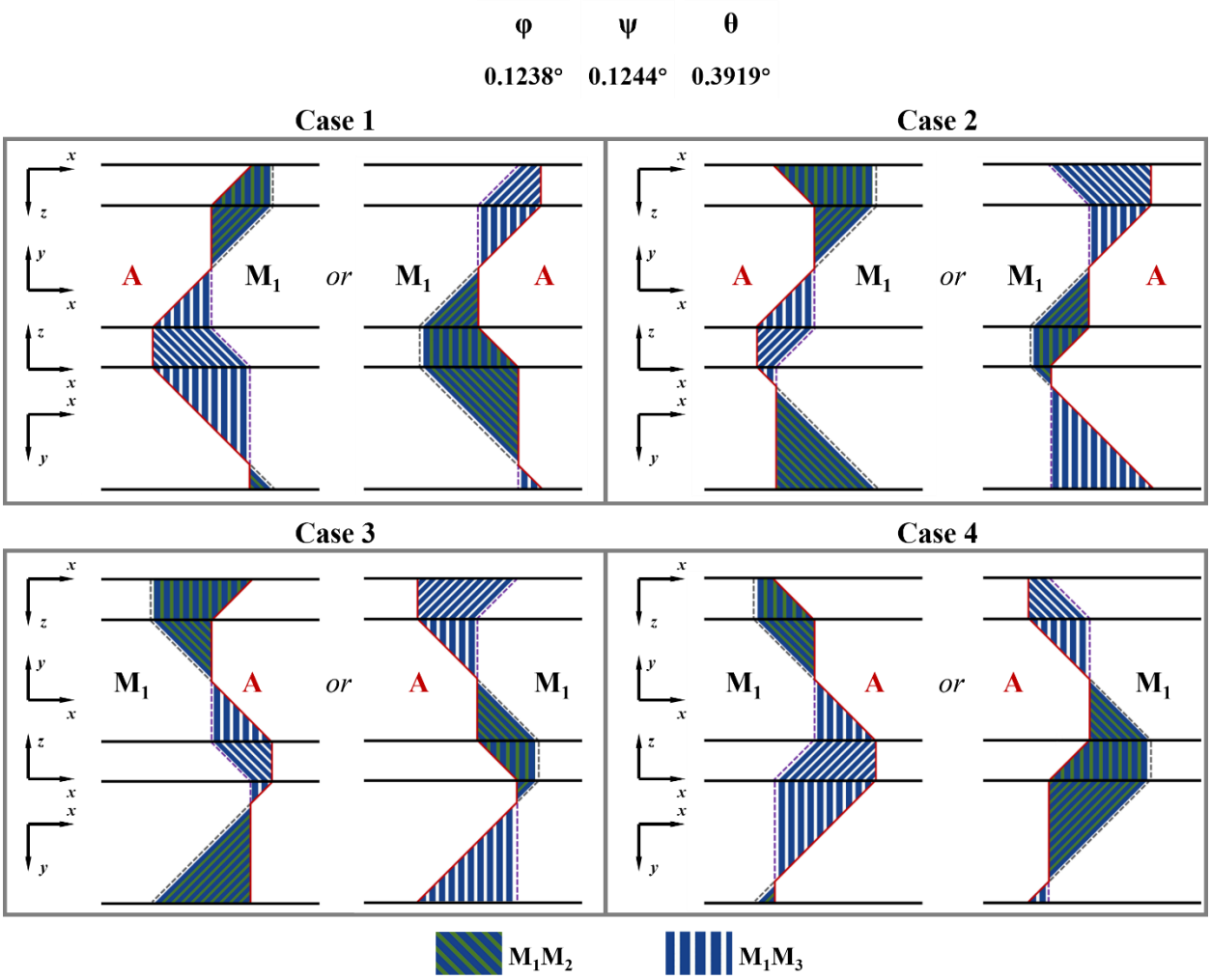

Fig. B3 The schematics for the optimal cases of the four-domain structure with small non-compatibility indicators.

Appendix C

The three martensite variants M_1, M_2, and M_3, whose short axes are along the *x*-, *y*- and *z*-coordinates respectively, are shown in Fig. 2(a). In this study, since the utilized lattice parameters are: martensite long axis $a \approx 5.95$ Å, martensite short axis $c \approx 5.61$ Å, and austenite characteristic length $a_0 \approx 5.84$ Å (Murray et al., 2000; Heczko et al., 2002; Zhang et al., 2018a), taking the austenite as the reference, the martensite variants have the strains of –4% and +2% along their short- and long-axis. Therefore, the transformation strains of the three variants can be obtained: M_1 ($\varepsilon_{xx} \approx -4\%$, $\varepsilon_{yy} \approx 2\%$, and $\varepsilon_{zz} \approx 2\%$), M_2 ($\varepsilon_{xx} \approx 2\%$, $\varepsilon_{yy} \approx -4\%$, and $\varepsilon_{zz} \approx 2\%$), and M_3 ($\varepsilon_{xx} \approx 2\%$, $\varepsilon_{yy} \approx 2\%$, and $\varepsilon_{zz} \approx -4\%$). If we denote the volume fraction of variant M_1, M_2, and M_3 as f_{M_1}, f_{M_2} and f_{M_3} respectively, there is a relation between these volume fractions in a fully martensitic zone:

$$f_{M_1} + f_{M_2} + f_{M_3} = 1 \tag{C.1}$$

Based on optical images on the specimen's *x*-*y* plane, the two local strain components ε_{xx} and ε_{yy} have been measured by DIC analysis using software VIC-2D. The relationship between the measured strain components (ε_{xx} and ε_{yy}) and the volume fractions (f_{M_1}, f_{M_2}, and f_{M_3}) can be derived as:

$$\begin{cases} \varepsilon_{xx} = -0.04\, f_{M_1} + 0.02\, f_{M_2} + 0.02\, f_{M_3} \\ \varepsilon_{yy} = 0.02\, f_{M_1} - 0.04\, f_{M_2} + 0.02\, f_{M_3} \end{cases} \tag{C.2}$$

Combining Eqs. (C.1) and (C.2), the volume fractions can be expressed as a function of ε_{xx} and ε_{yy}:

$$\begin{cases} f_{M_1} = \frac{0.02 - \varepsilon_{xx}}{0.06} \\ f_{M_2} = \frac{0.02 - \varepsilon_{yy}}{0.06} \\ f_{M_3} = \frac{0.02 + \varepsilon_{xx} + \varepsilon_{yy}}{0.06} \end{cases} \tag{C.3}$$

As the laminates in the domain II in Fig. 2 are very fine, we would like to confirm the volume fractions of martensite variants in this domain by the DIC stain measurements and the above Eq.

(C3). Figure C1 shows the strain distribution over a specific region (yellow dotted area) occupied successively by the single variant M_3, the domain II and the austenite, corresponding sequentially to the Frames (i), (ii) and (iii) respectively from Movie 3. For the DIC processing, taking the austenite as the reference state (ε_{xx} = 0%, ε_{yy} = 0%), the measured strain components of the domain II are $\varepsilon_{xx} \approx 2\%$ and $\varepsilon_{yy} \approx 0\%$, which are combined with Eq. (C.3) to give the volume fractions $f_{\mathrm{M}_1} = 0$, $f_{\mathrm{M}_2} = 1/3$, and $f_{\mathrm{M}_3} = 2/3$. That means, the domain II is a twin consisting of M_3 and M_2 with the volume ratio ≈ 2:1. Such a result is consistent with the compatibility analysis (in Fig. 3) and the observed orientation of the habit plane and twin boundaries (in Fig. 2).

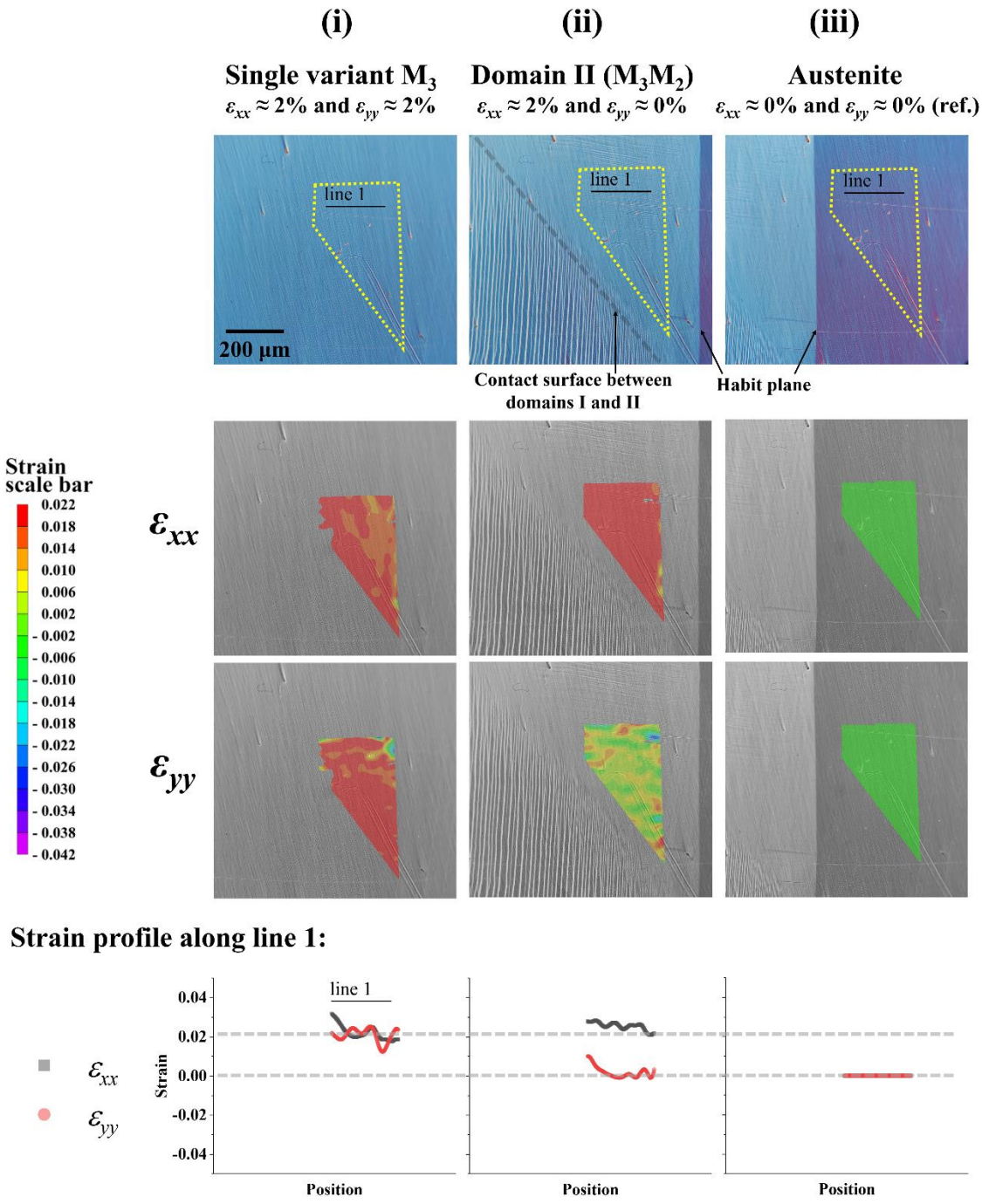

Fig. C1. The DIC strain maps and the associated strain profiles of a region (yellow dotted area) occupied by the single variant M_3, the domain II (defined in Fig. 2) and the austenite sequentially in the Frames (i), (ii) and (iii) respectively from Movie 3 (corresponding to the time moments 0s, 12.14s, and 14.32s, respectively).

Reference:

Abeyaratne, R., Knowles, J.K., 1991. Kinetic relations and the propagation of phase boundaries in solids. Archive for Rational Mechanics and Analysis 114, 119-154.

Arndt, M., Griebel, M., Novák, V., Roubíček, T., Šittner, P., 2006. Martensitic transformation in NiMnGa single crystals: Numerical simulation and experiments. Int. J. Plasticity 22, 1943-1961.

Balandraud, X., Delpueyo, D., Grédiac, M., Zanzotto, G., 2010. Almost compatible microstructures in shape memory alloys. Acta Mater. 58, 4559-4577.

Balandraud, X., Zanzotto, G., 2007. Stressed microstructures in thermally induced M9R–M18R martensites. J. Mech. Phys. Solids 55, 194-224.

Ball, J.M., Carstensen, C., 1997. Nonclassical Austenite-Martensite Interfaces. J. Phys. IV France 07, C5-35-C35-40.

Ball, J.M., James, R.D., 1989. Fine phase mixtures as minimizers of energy. Springer, Berlin, Heidelberg.

Ball, J.M., James, R.D., 1992. Proposed experimental tests of a theory of fine microstructure and the two-well problem. Philosophical Transactions of the Royal Society of London. Series A: Physical and Engineering Sciences 338, 389-450.

Barsh, G.R., Krumhansl, J.A., 1984. Twin boundaries in ferroelastic media without interface dislocations. Physical Review Letters 53, 1069-1072.

Basinski, Z.S., Christian, J.W., 1954. Experiments on the martensitic transformation in single crystals of indium-thallium alloys. Acta Metall. 2, 148-159, 161-166.

Bhattacharya, K., 1991. Wedge-like microstructure in martensites. Acta Metall. 39, 2431-2444.

Bhattacharya, K., 1992. Self-accommodation in martensite, Arch. Rational Mech. Anal., pp. 201-244.

Bhattacharya, K., 2003. Microstructure of Martensite: Why it Forms and How it Gives Rise to the Shape-memory Effect. Oxford University Press, Oxford.

Bowles, J.S., 1951. The crystallographic mechanism of the martensite reaction in iron-carbon alloys. Acta Crystallogr. 4, 162-171.

Bowles, J.S., Mackenzie, J.K., 1954. The crystallography of martensite transformations I. Acta Metall. 2, 129-137.

Bronstein, E., Faran, E., Shilo, D., 2019. Analysis of austenite-martensite phase boundary and twinned microstructure in shape memory alloys: The role of twinning disconnections. Acta Mater. 164, 520-529.

Bruno, N.M., Wang, S., Karaman, I., Chumlyakov, Y.I., 2017. Reversible Martensitic Transformation under Low Magnetic Fields in Magnetic Shape Memory Alloys. Scientific reports 7, 40434.

Chang, L.C., Read, T.A., 1951. Plastic deformation and diffusionless phase changes in metals — The Gold-Cadmium beta phase. Journal of Metals 3, 47-52.

Chen, X., He, Y.J., 2020. Thermo-magneto-mechanical coupling dynamics of magnetic shape memory alloys. Int. J. Plasticity 129, 102686.

Chen, X., Moumni, Z., He, Y.J., Zhang, W., 2014. A three-dimensional model of magneto-mechanical behaviors of martensite reorientation in ferromagnetic shape memory alloys. J. Mech. Phys. Solids 64, 249-286.

Chen, X., Srivastava, V., Dabade, V., James, R.D., 2013. Study of the cofactor conditions:

Conditions of supercompatibility between phases. J. Mech. Phys. Solids 61, 2566-2587.
Christian, J.W., 1982. Deformation by moving interfaces. Metallurgical Transactions A 13, 509-538.
Chulist, R., Straka, L., Lanska, N., Soroka, A., Sozinov, A., Skrotzki, W., 2013. Characterization of mobile type I and type II twin boundaries in 10M modulated Ni–Mn–Ga martensite by electron backscatter diffraction. Acta Mater. 61, 1913-1920.
Cisse, C., Zaki, W., Zineb, T.B., 2016. A review of constitutive models and modeling techniques for shape memory alloys. Int. J. Plasticity 76, 244-284.
Cui, J., Chu, Y.S., Famodu, O.O., Furuya, Y., Hattrick-Simpers, J., James, R.D., Ludwig, A., Thienhaus, S., Wuttig, M., Zhang, Z., Takeuchi, I., 2006. Combinatorial search of thermoelastic shape-memory alloys with extremely small hysteresis width. Nat Mater 5, 286-290.
Duval, A., Haboussi, M., Ben Zineb, T., 2011. Modelling of localization and propagation of phase transformation in superelastic SMA by a gradient nonlocal approach. Int. J. Solids struct. 48, 1879-1893.
Ericksen, J.L., 1975. Equilibrium of bars. Journal of Elasticity 5, 191-201.
Ericksen, J.L., 1980. Some phase transitions in crystals. Acrchive for Rotaional Mechanics and Analysis 73, 99-124.
Falk, F., 1980. Model free energy, mechanics, and thermodynamics of shape memory alloys. Acta Metall. 28, 1773-1780.
Faran, E., Shilo, D., 2011. The kinetic relation for twin wall motion in NiMnGa. J. Mech. Phys. Solids 59, 975-987.
Faran, E., Shilo, D., 2015. Multi-Scale Dynamics of Twinning in SMA. Shap. Mem. Superelasticity 1, 180-190.
Glatz, O., Seiner, H., Landa, M., 2009. FEM Modelling of Elastically Strained Interfacial Microstructures in Cu-Al-Ni Single Crystals, ESOMAT 2009 - 8th European Symposium on Martensitic Transformations.
Glavatska, N., Ullakko, K., 2001. X-Ray Diffraction Study of the Effect of a Magnetic Field on the Martensitic Transformation in Ni₂MnGa Alloys. Materials Science Forum 378-381, 420-425.
Glavatska, N.I., Ullakko, K., 2000. Isomagnetic martensitic transformation in Ni_2MnGa alloys. J. Magn. Magn. Mater. 218, 256-260.
Gu, H., Bumke, L., Chluba, C., Quandt, E., James, R.D., 2018. Phase engineering and supercompatibility of shape memory alloys. Materials Today 21, 265-277.
Haldar, K., Lagoudas, D.C., Karaman, I., 2014. Magnetic field-induced martensitic phase transformation in magnetic shape memory alloys: Modeling and experiments. J. Mech. Phys. Solids 69, 33-66.
Hallai, J.F., Kyriakides, S., 2013. Underlying material response for Lüders-like instabilities. Int. J. Plasticity 47, 1-12.
Hane, K.F., 1999. Bulk and thin film microstructures in untwinned martensites. J. Mech. Phys. Solids 47, 1917-1939.
Hane, K.F., Shield, T.W., 1998. Symmetry and microstructure in martensites. Philos. Mag. A 78, 1215-1252.
Hane, K.F., Shield, T.W., 1999a. Microstructure in a copper—aluminium—nickel shape–memory alloy. Proceedings of the Royal Society A 455, 3910-3915.
Hane, K.F., Shield, T.W., 1999b. Microstructure in the cubic to monoclinic transition in titanium–nickel shape memory alloys. Acta Mater. 47, 2603-2617.

Hane, K.F., Shield, T.W., 2000a. Microstructure in a Cubic to Orthorhombic Transition. Journal of elasticity and the physical science of solids 59, 267-318.
Hane, K.F., Shield, T.W., 2000b. Microstructure in the cubic to trigonal transition. Mat. Sci. Eng. A-Struct. 291, 147-159.
He, Y.J., 2023. Interface propagation and energy dissipation in Shape Memory Alloys. Scripta Mater. 230.
He, Y.J., Sun, Q.P., 2009. Effects of structural and material length scales on stress-induced martensite macro-domain patterns in tube configurations. Int. J. Solids struct. 46, 3045-3060.
Heczko, O., Lanska, N., Soderberg, O., Ullakko, K., 2002. Temperature variation of structure and magnetic properties of Ni–Mn–Ga magnetic shape memory alloys. J. Magn. Magn. Mater. 242-245, 1446-1449.
Heczko, O., Seiner, H., Stoklasová, P., Sedlák, P., Sermeus, J., Glorieux, C., Backen, A., Fähler, S., Landa, M., 2018. Temperature dependence of elastic properties in austenite and martensite of Ni-Mn-Ga epitaxial films. Acta Mater. 145, 298-305.
Heczko, O., Straka, L., Seiner, H., 2013. Different microstructures of mobile twin boundaries in 10M modulated Ni–Mn–Ga martensite. Acta Mater. 61, 622-631.
Heczko, O., Veřtát, P., Vronka, M., Kopecky, V., Perevertov, O., 2016. Ni–Mn–Ga Single Crystal Exhibiting Multiple Magnetic Shape Memory Effects. Shap. Mem. Superelasticity 2, 272-280.
James, R.D., 1980. The propagation of phase boundaries in elastic bars. Arch. Ration. Mech. Anal. 73, 125-158.
James, R.D., Hane, K.F., 2000. Martensitic Transformations and shape-memory materials. Acta Mater. 48, 197-222.
James, R.D., Kohn, R.V., Shield, T.W., 1995a. Modeling of Branched Needle Microstructures at the Edge of a Martensite Laminate. J. Phys. IV France 05, C8-253-C258-259.
James, R.D., Kohn, R.V., Shield, T.W., 1995b. Modeling of Branched Needle Microstructures at the Edge of a Martensite Laminate. J. Phys. IV France 05, C8-253-C258-259.
Kamarád, J., Albertini, F., Arnold, Z., Fabbrici, S., Kaštil, J., 2014. Extraordinary magnetic and structural properties of the off-stoichiometric and the Co-doped Ni 2 MnGa Heusler alloys under high pressure. Acta Mater. 77, 60-67.
Karaca, H., Karaman, I., Basaran, B., Chumlyakov, Y., Maier, H., 2006. Magnetic field and stress induced martensite reorientation in NiMnGa ferromagnetic shape memory alloy single crystals. Acta Mater. 54, 233-245.
Karaman, I., Karaca, H.E., Basaran, B., Lagoudas, D.C., Chumlyakov, Y.I., Maier, H.J., 2006. Stress-assisted reversible magnetic field-induced phase transformation in Ni2MnGa magnetic shape memory alloys. Scripta Mater. 55, 403-406.
Khachaturyan, A.G., 1983. Theory of structural transformations in solids. Courier Corporation.
Kiefer, B., Lagoudas, D.C., 2005. Magnetic field-induced martensitic variant reorientation in magnetic shape memory alloys. Philosophical Magazine 85, 4289-4329.
Krumhansl, J.A., Gooding, R.J., 1989. Structural phase transitions with little phonon softening and first-order character. Phys Rev B Condens Matter 39, 3047-3053.
Levitas, V.I., Lee, D.-W., Preston, D.L., 2010. Interface propagation and microstructure evolution in phase field models of stress-induced martensitic phase transformations. Int. J. Plasticity 26, 395-422.
M. Pitteri, Zanzotto, G., 1998. Generic and non-generic cubic-to-monoclinic transitions and their twins. Acta Mater. 46, 225-237.
Mañosa, L., Gonzàles-Comas, A., Obrado, E., Planes, A., Chernenko, V.A., Kokorin, V.V., Cesari,

E., 1997. Anomalies related to the TA_2-phonon-mode condensation in Heusler Ni2MnGa alloy. Phys. Rev. B 55, 11068-11071.
Müller, I., 1989. On the size of the hysteresis in pseudoelasticity. Continuum mechanics and thermodynamics 1, 125-142.
Müller, I., Xu, H., 1991. On the pseudo-elastic hysteresis. Acta Metallurgica et Materialia 39, 263-271.
Murray, S.J., Marioni, M., Allen, S.M., O'Handley, R.C., Lograsso, T.A., 2000. 6% magnetic-field-induced strain by twin-boundary motion in ferromagnetic Ni–Mn–Ga. Appl. Phys. Lett. 77, 886-888.
Otsuka, K., Shimizu, K.i., 1974. Morphology and Crystallography of Thermoelastic Cu–Al–Ni Martensite Analyzed by the Phenomenological Theory. Transactions of the Japan Institute of Metals 15, 103-108.
Otsuka, K., Wayman, C.M., 1998. Shape memory materials. Chambridge University Press.
Pascan, O.Z., He, Y.J., Moumni, Z., Zhang, W.H., 2015. Temperature rise of high-frequency martensite reorientation via Type II twin boundary motion in NiMnGa Ferromagnetic Shape Memory Alloy. Scripta Mater. 104, 71-74.
Peng, Q., He, Y.J., Moumni, Z., 2015. A phase-field model on the hysteretic magneto-mechanical behaviors of ferromagnetic shape memory alloy. Acta Mater. 88, 13-24.
Petryk, H., Stupkiewicz, S., 2010. Interfacial energy and dissipation in martensitic phase transformations. Part I: Theory. J. Mech. Phys. Solids 58, 390-408.
Pitteri, M., 1984. Reconciliation of local and global symmetries of crystals. Journal of Elasticity 14, 175-190.
Pitteri, M., Zanzotto, G., 2002. Continuum models for phase transitions and twinning in crystals. Chapman and Hall/CRC.
Planes, A., Mañosa, L., Moya, X., Krenke, T., Acet, M., Wassermann, E.F., 2007. Magnetocaloric effect in Heusler shape-memory alloys. J. Magn. Magn. Mater. 310, 2767-2769.
Qin, G., Zhang, C., Zhang, S., Chen, X., He, Y.J., 2023. Compatibility effect on stress-free two-way memory of Ni-Mn-Ga single crystal. J. Alloy Compd. 935.
Rogovoy, A., Stolbova, O., 2016. Modeling the magnetic field control of phase transition in ferromagnetic shape memory alloys. Int. J. Plasticity 85, 130-155.
Roitburd, A.L., 1978. Martensitic Transformation as a Typical Phase Transformation in Solids, pp. 317-390.
Ruddock, G., 1994. A Microstructure of Martensite which is not a Minimiser of Energy: the X-Interface. Arch. Rational Mech. Anal. 127, 1-39.
Saburi, T., Wayman, C.M., 1979. Crystallographic similarities in shape memory martensites. Acta Metall. 27, 979-995.
Salzbrenner, R.J., Cohen, M., 1979. On the thermodynamics of thermoelastic martensitic transformations. Acta Metall. 27, 739-748.
Segui, C., Cesari, E., Pons, J., Chernenko, V.A., Kokorin, V.V., 1996. A Premartensitic Anomaly in Ni2MnGa Alloys Studied by Dynamic Mechanical Analysis. J. Phys. IV France 06, C8-381-C388-384.
Sehitoglu, H., Wang, J., Maier, H.J., 2012. Transformation and slip behavior of Ni2FeGa. Int. J. Plasticity 39, 61-74.
Seiner, H., 2015. Mobile Interfacial Microstructures in Single Crystals of Cu–Al–Ni Shape Memory Alloy. Shap. Mem. Superelasticity 1, 268-274.
Seiner, H., Glatz, O., Landa, M., 2009. Interfacial Microstructures in Martensitic Transitions: From

Optical Observations to Mathematical Modeling. International Journal of Multiscale Computational Engineering 7, 445-456.
Seiner, H., Landa, M., 2009. Non-classical austenite-martensite interfaces observed in single crystals of Cu–Al–Ni. Phase Transitions 82, 793-807.
Seiner, H., Plucinsky, P., Dabade, V., Benešová, B., James, R.D., 2020. Branching of twins in shape memory alloys revisited. J. Mech. Phys. Solids 141.
Seiner, H., Sedlák, P., Landa, M., 2008. Shape recovery mechanism observed in single crystals of Cu–Al–Ni shape memory alloy. Phase Transitions 81, 537-551.
Seiner, H., Straka, L., Heczko, O., 2014. A microstructural model of motion of macro-twin interfaces in Ni–Mn–Ga 10M martensite. J. Mech. Phys. Solids 64, 198-211.
Shield, T.W., 1995. Orientation dependence of the pseudoelastic behavior of single crystals of Cu-Al-Ni in tension. J. Mech. Phys. Solids 43, 869-895.
Shusong Tan, Xu, H., 1990. Observations on a CuAlNi single crystal. Continuum mechanics and thermodynamics 2, 241-244.
Straka, L., Heczko, O., Seiner, H., Lanska, N., Drahokoupil, J., Soroka, A., Fähler, S., Hänninen, H., Sozinov, A., 2011. Highly mobile twinned interface in 10M modulated Ni–Mn–Ga martensite: Analysis beyond the tetragonal approximation of lattice. Acta Mater. 59, 7450-7463.
Stupkiewicz, S., Górzyńska-Lengiewicz, A., 2012. Almost compatible X-microstructures in CuAlNi shape memory alloy. Continuum Mechanics and Thermodynamics 24, 149-164.
Stupkiewicz, S., Maciejewski, G., Petryk, H., 2007. Low-energy morphology of the interface layer between austenite and twinned martensite. Acta Mater. 55, 6292-6306.
Stupkiewicz, S., Maciejewski, G., Petryk, H., 2012. Elastic micro-strain energy of austenite–martensite interface in NiTi. Modelling and Simulation in Materials Science and Engineering 20.
Stupkiewicz, S., Rezaee-Hajidehi, M., Petryk, H., 2021. Multiscale analysis of the effect of interfacial energy on non-monotonic stress–strain response in shape memory alloys. Int. J. Solids struct. 221, 77-91.
Sun, Q.P., He, Y.J., 2008. A multiscale continuum model of the grain-size dependence of the stress hysteresis in shape memory alloy polycrystals. Int. J. Solids struct. 45, 3868-3896.
Wechsler, M.S., Lieberman, D.S., Read, T.A., 1953. On the theory of the formation of martensite. J. Metall./Trans. AIME 197, 1503-1515.
Wollants, P., Roos, J.R., Delaey, L., 1993. Thermally- and stress-induced thermoelastic martensitic transformations in the reference frame of equilibrium thermodynamics. Progress in Materials Science 37, 227-288.
Yin, R., Wendler, F., Krevet, B., Kohl, M., 2016. A magnetic shape memory microactuator with intrinsic position sensing. Sensors and Actuators A: Physical 246, 48-57.
Zhang, C., Qin, G., Zhang, S., Chen, X., He, Y.J., 2023. Hysteresis effect on austenite-martensite interface in Ni-Mn-Ga single crystal. Scripta Mater. 222.
Zhang, S., Chen, X., Moumni, Z., He, Y.J., 2018a. Coexistence and compatibility of martensite reorientation and phase transformation in high-frequency magnetic-field-induced deformation of Ni-Mn-Ga single crystal. Int. J. Plasticity 110, 110-122.
Zhang, S., Chen, X., Moumni, Z., He, Y.J., 2018b. Thermal effects on high-frequency magnetic-field-induced martensite reorientation in ferromagnetic shape memory alloys: An experimental and theoretical investigation. Int. J. Plasticity 108, 1-20.
Zhang, S., Qin, G., He, Y.J., 2020. Ambient effects on the output strain of Ni–Mn-Ga single crystal magnetic shape memory alloy. J. Alloy Compd. 835, 155159.

Zhang, Z., James, R.D., Müller, S., 2009. Energy barriers and hysteresis in martensitic phase transformations. Acta Mater. 57, 4332-4352.
Zreihan, N., Faran, E., Shilo, D., 2015. The effects of temperature on the lattice barrier for twin wall motion. Appl. Phys. Lett. 107.